5-1-2012

Water breakthrough behavior and GDL degradation mechanisms in a PEM fuel cell

Matthew Garofalo

Water Breakthrough Behavior and GDL Degradation Mechanisms in a PEM Fuel Cell

By

Matthew L. Garofalo

A Thesis Submitted in Partial Fulfillment of the Requirement for Master of Science in Mechanical Engineering

Approved By:

Department of Mechanical Engineering Committee

Dr. Satish G. Kandlikar - Thesis Advisor _____

Dr. Robert J. Stevens _____

Dr. Mario W. Gomes _____

Dr. Agamemnon L. Crassidis _____

Rochester Institute of Technology
New York 14623
May, 2012

PERMISSION TO REPRODUCE THE THESIS

TITLE OF THESIS:

Water Breakthrough Behavior and GDL Degradation Mechanisms in a PEM Fuel Cell

I, Matthew L. Garofalo, hereby grant permission to the Wallace Memorial Library of Rochester Institute of Technology to reproduce my thesis in the whole or part. Any reproduction will not be for commercial use or profit.

Date: _____ Name: _____

ACKNOWLEDGEMENTS

This work would have not been possible without the supervision, guidance, and never ending support from my advisor, Dr. Satish Kandilkar. I would like to express my most sincere gratitude to him for providing me with the unique opportunity of working with him in his research lab.

I would also like to thank my fellow members of the Thermal Analysis, Microfluidics, and Fuel Cell Laboratory for their friendship, dependability, advice, and encouragement. They provided a very welcoming and professional work setting that allowed for me to perform to the best of my abilities. This made for a very insightful and enlightening experience.

Generous help from Robert Kraynik and Dave Hathaway was provided during the manufacturing processes of the experimental setup components and I would like to thank them for all they've done. The superior craftsmanship of the setup would not have been possible without their patience, advice, and expertise. The Department of Mechanical Engineering was also there for me every step of the way and helped extensively in choosing the right pathways for my research and degree and I greatly appreciate all the help.

David Pawlik, a Microelectronic Engineering Phd. student, took time away from his very busy schedule to help perform the compositional analysis and I really appreciate his generosity.

Finally, I would like to send a heartfelt thank you to my mother, father, and brother for always believing in me and giving me all the support, love, and encouragement I could ever need. I would like to dedicate this work to my father who passed away just before the start of my research. If it wasn't for him, this work would never have been made possible.

ABSTRACT

The water that exists within the porous components of a proton exchange membrane fuel cell (PEMFC) during operation affects the performance characteristics of the fuel cell. The water transport processes through the gas diffusion layer (GDL) and microporous layer (MPL) are suspected to change over the cell lifetime due to material degradation mechanisms. The understanding of how GDL degradation affects its water transport mechanisms is needed so that GDL and MPL material can be optimized for maximum PEMFC performance and durability. One of these water transport mechanisms is capillary action. Measuring the capillary breakthrough pressure (CBP) is a novel characterization method where water is delivered to an initially dry GDL sample at a low flow rate. Studying the dynamic capillary pressure (DCP) can add insight to how the water is emerging out of the GDL. Various ex situ experiments have been conducted involving the study of the water breakthrough dynamics inherent to different GDLs. However, these experiments have only been performed on fresh GDLs. A novel ex situ test section was designed to not only degrade GDLs but also to measure the CBP before and after the degradation process. The GDLs were degraded by being exposed to simulated conditions seen at the cathode side of a PEMFC. These conditions included electric current, temperature, compression, and accelerated liquid water flow and were applied to the samples for prolonged periods of time. Degradation mechanisms were identified through the use of CBP measurement and DCP observation, surface wettability measurement, confocal laser scanning microscopy, and compositional analysis on the GDL samples before and after degradation.

CONTENTS

LIST OF FIGURES

LIST OF TABLES

NOMENCLATURE

Symbols:

ε	= Porosity (%)
θ	= contact angle (°)
μ	= Dynamic viscosity (Pa s)
ξ	= Electrical resistivity (Ω m)
ρ	= Density (kg m^{-3})
σ	= Surface tension (N m^{-1})
A	= Area (m^2)
Ca	= Capillary number
F	= Faraday's constant (C mol^{-1})
I	= Current (A)
j	= Current density (A m^{-2})
J(s)	= Leverett function
K	= Darcy coefficient
L	= GDL thickness (m)
M	= Viscosity Ratio
$\dot{m}$	= Mass flow rate (kg s^{-1})
MW	= Molecular weight (kg mol^{-1})
n	= Equivalent electrons per mole of reactant (eq mol^{-1})
P	= Pressure (Pa)
Q	= Volumetric flow rate (m^3 s^{-1})
R	= Resistance (Ω)

r = Radius (m)

s = Saturation (%)

T = Temperature (K)

t = Time (s)

u = Velocity ($m\ s^{-1}$)

V = Voltage (V)

~~V~~ = Volume (m^3)

Subscripts:

Air = Air

b = Bulk

c = Capillary

H_2O = Water

nw = Nonwetting

s = Solid phase

u = Uncompressed

w = Wetting

ABBREVIATIONS

ACL	- Anode Catalyst Layer
CBP	- Capillary Breakthrough Pressure
CCL	- Cathode Catalyst Layer
CLSM	- Confocal Laser Scanning Microscopy
DC	- Direct Current
DCP	- Dynamic Capillary Pressure
DI	- Deionized
EDX	- Energy Dispersive X-ray
FEP	- Fluorinated Ethylene Propylene
GDL	- Gas Diffusion Layer
HOR	- Hydrogen Oxidation Reaction
MEA	- Membrane Electrode Assembly
MPL	- Microporous Layer
ORR	- Oxygen Reduction Reaction
PAN	- Polyacrylonitrile
PDMS	- Polydimethylsiloxane
PEMFC	- Proton Exchange Membrane Fuel Cell

PTFE - Polytetrafluoroethylene

PU - Polyurethane

RH - Relative Humidity

SEM - Scanning Electron Microscope

TGA - Thermo-gravimetric Analysis

TPB - Triple-phase Boundary

1. INTRODUCTION

The desire to reduce the dependence of the automobile on petroleum as well as the emission of harmful automobile exhaust into the atmosphere has pressured government agencies and the automotive industry to extensively seek an alternative to the internal combustion engine. Renewable hydrogen fuel has gained much popularity and is capable of being generated by water electrolysis. If the power supplied for electrolysis is from a renewable resource, such as hydroelectric power, the entire process becomes sustainable. Proton exchange membrane fuel cells (PEMFCs) have substantial potential to utilize hydrogen fuel and power tomorrow's automobiles with additional favorable characteristics such as zero carbon emissions, high operation efficiency, and high power density. Automotive PEMFCs must be able to withstand dynamic loads, long strenuous run times, and harsh operation environments as part of a vehicle powertrain. One of the main issues that must be overcome before PEMFC powertrains can be introduced to the automotive market is their limited lifetime. In turn, major government programs including the United States Department of Energy, the European Commission, and Japan's Ministry of Economy call for PEMFC durability research. The 2015 PEMFC transportation durability target set forth by all three organizations is 5000 hours [1]. The ideal operating conditions for maximum durability in PEMFCs include steady state load, close to 100% relative humidity (RH), and temperatures near 75 °C [2]. Well designed fuel cells can last over 40,000 hours under ideal conditions. One of the most popular degradation mechanisms suspected to cause performance loss is the loss of hydrophobicity of the gas diffusion layer (GDL) [2]. Therefore a thorough understanding of the GDL and both its water transport and degradation mechanisms plays a very important role in maximizing the lifetime and performance of PEMFCs.

PEMFCs are electrochemical energy conversion devices. Electrochemical energy is converted into electrical energy, water, and waste heat through simultaneous reduction and oxidation, or redox reactions. Although methanol and alcohol can be used in some PEMFCs, hydrogen is the most favorable fuel as its reaction with oxygen yields only water rather than water and carbon dioxide. In a PEMFC fueled with hydrogen, a hydrogen oxidation reaction (HOR) and oxygen reduction reaction (ORR) occurs at the anode and cathode electrodes respectively. Figure 1 shows a basic schematic of the different components that make up a single fuel cell as well as the flow paths for the hydrogen, oxygen, water, and electricity. A purified air stream is typically supplied at the cathode and the oxygen inherent to the air is utilized in the ORR. Equations (1) and (2) describe the HOR and ORR respectively.

$$H_2 \rightarrow 2H^+ + 2e^- \quad (1)$$

$$\frac{1}{2}O_2 + 2H^+ + 2e^- \rightarrow H_2O \quad (2)$$

The overall reaction is therefore

$$H_2 + \frac{1}{2}O_2 \rightarrow H_2O + heat + electric\ energy \quad (3)$$

In a single PEMFC, hydrogen fuel is supplied to the anode side of the fuel cell via the unipolar plate, or flow field, channels and subsequently travels through the pore network of the GDL to the anode catalyst layer (ACL) where the HOR reaction occurs. As Figure 1 shows, the catalyst layer facing side of the GDL may have a thin microporous layer (MPL) added for various performance enhancements. The hydrogen protons, $2H^+$, yielded by the HOR reaction at the ACL are conducted across the membrane, or electrolyte. The electrons are turned away from the membrane as it is only conductive to the hydrogen protons and

instead are conducted back through the solid parts of the anode GDL. Subsequently, they move through the electrically conductive anode flow field solid material which, in turn, directs them through an external load before returning to the cathode. At the cathode, air is passed through the flow field and oxygen from the air diffuses through the GDL to the cathode catalyst layer (CCL). At the CCL, the hydrogen protons and electrons coming from the electrolyte and external circuit respectively meet the oxygen and, in turn, cause the ORR. The water produced exits the cell via the cathode GDL and adjacent flow field. The heat produced is conducted out through the solid portions of the GDL and flowfields. Water will also exist on the anode side due to the humidification of the incoming hydrogen stream. Water molecules are dragged across the membrane due to a polar attraction that exists between the molecules and the positively charged hydrogen protons [3]. The cathode incoming air stream can also be humidified.

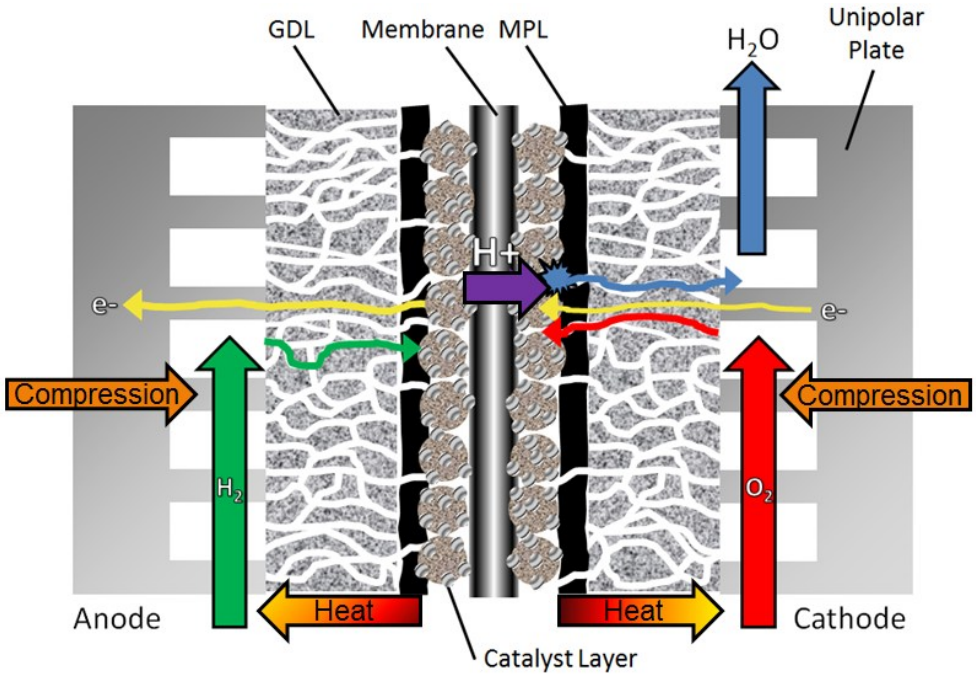

Figure 1: Basic schematic of a PEMFC including GDL and MPL locations.

The ACL, membrane, and CCL are collectively referred to as the catalyst coated membrane or membrane electrode assembly (MEA). It can also be deduced from Figure 1 that the GDL has many functions within a PEMFC. In summary it distributes hydrogen and oxygen reactant gases to the catalyst layers, transports water away from the catalyst layers, and conducts electrons and heat. In addition to these duties it is also corrosion resistant and provides mechanical support for the thin and flexible catalyst layers and electrolyte. All these duties provide different mechanisms towards the eventual degradation of the GDL.

There have been many degradation studies conducted on the catalyst layers and electrolytes of PEMFC's as these components are critical to PEMFC operation. However, the durability testing of secondary components such as the GDL should also be investigated as they can also affect PEMFC performance. GDL and MPL degradation mechanisms can be identified by a number of different methods. The capillary breakthrough pressure (CBP), or the capillary pressure required for liquid water to break through a dry GDL specimen, is expected to change with respect to degradation. The dynamic capillary pressure (DCP), or the recurrent pressure spikes that occur after the CBP value is reached, is also expected to change. The CBP and DCP have been investigated previously, but only on fresh GDLs. This work investigates the degradation mechanisms of the GDL and MPL by subjecting them to a degradation test that consists of simulating the following operation conditions seen at a PEMFC cathode for extended amounts of time:

i. Typical current density
ii. Accelerated liquid water flow rate
iii. Typical compression
iv. Typical operation temperature

In turn, the CBP and DCP were investigated before and after the GDLs were degraded. Surface morphology changes of both the GDL and MPL due to the degradation test were observed through the use of a confocal laser scanning microscope (CLSM). The surface wettability of the MPL side and fibrous side of the GDL was measured in specific locations using a contact angle measurement system before and after the degradation test was carried out. A compositional analysis was also performed on one of the GDL samples to identify changes in the elemental makeup of the GDL caused by the degradation test. There are many comparisons that can be made as well as conclusions that can be drawn from these tests, and measurements. The resulting information can be used to further understand the degradation mechanisms in GDLs and can aid in the development of future GDLs for PEMFC applications. This will clarify even further the viability of PEMFCs in the auto industry.

1.1 Gas Diffusion Layer

1.1.1 Role in a PEMFC

The liquid water produced in a fuel cell must be quickly exited from the CCL where it is produced to maintain clear entrance pathways for more reactant gas to reach active sites on the CCL. This results in gas and liquid phases competing to occupy the same pores of the catalyst layers and the GDL which, in turn, affects mass transport in the fuel cell.

The GDL is a porous and electrically conductive material that is a very important component of a PEMFC and has six main functions:

i. Electron conduction
ii. Water transport
iii. Reactant transport

iv. Structural support for membrane and catalyst layers

v. Heat conduction

vi. Corrosion resistance

The focus of this work will be on carbon fiber based GDLs as they are the most popular type of GDL due to their high porosity (≥ 70%) at a pore size of 10-30 μm and high electrical conductivity [4]. Carbon fiber GDLs can be constructed as a non-woven paper, woven cloth, or woven felt. The fuel cell industry standard GDL is carbon paper as it is inexpensive and easy to apply MPLs or catalyst layers directly to [1]. This work will focus on carbon fiber paper GDLs for this reason. Figure 2 shows a CLSM image of a carbon paper GDL.

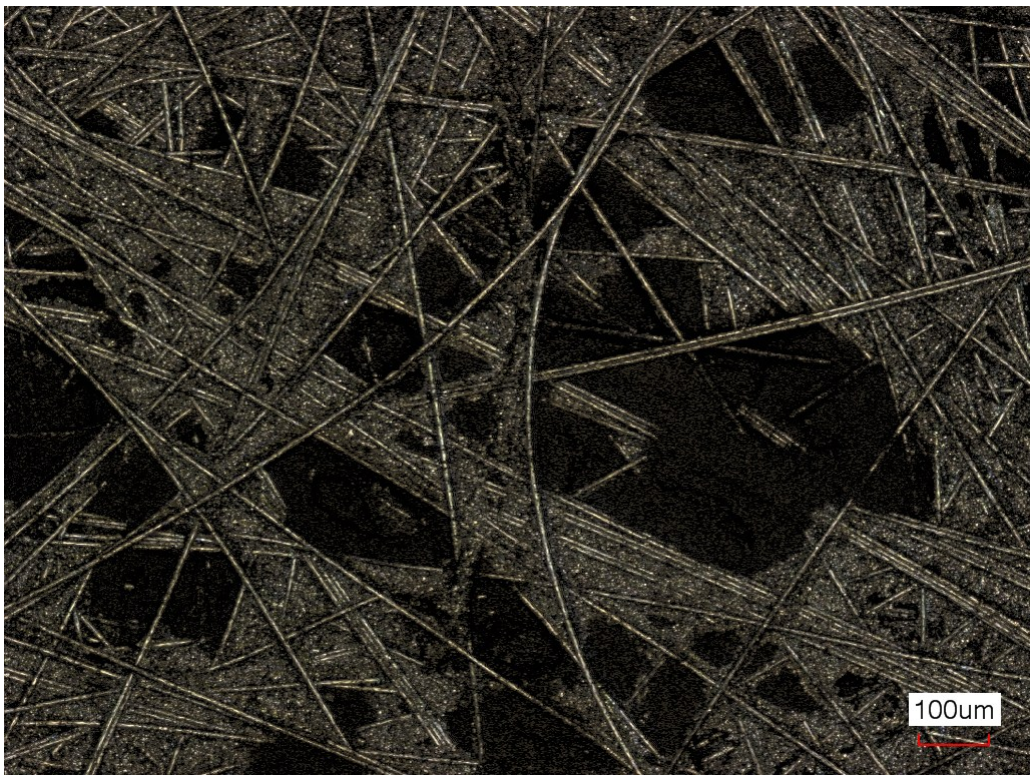

Figure 2: CLSM image of the GDL fiber structure (SGL Group Sigracet® 25BC).

1.1.2 Manufacturing Processes

The carbon fibers are typically a copolymer comprised of 90% or more polyacrylonitrile (PAN) with diameters on the order of 7 μm and can be manufactured by following a wet-laid or dry-laid production process [4]. The wet-laid manufacturing process for carbon paper GDLs has five main parts [1,4]:

i. Papermaking
ii. Impregnation
iii. Molding
iv. Carbonization
v. Graphitization

Papermaking consists of cutting the carbon fibers into specific lengths and subsequently putting them in a water bath with polyvinyl alcohol binders. A binder and carbon fiber dispersion forms and is then dried of water in an oven and is ready for impregnation with a thermoset phenolic resin from a methanol based solvent at this point [4]. Once, impregnated the resin is dried at 150 °C in open air, compression molded at 400-550 kPa and 175 °C, and finally cured at 200 °C in open air [4]. Carbonization and graphitization are the final steps in the manufacturing process and are performed in a furnace filled with inert gas and may be under vacuum. The fibers themselves are carbonized through exposure to high temperatures ranging from 1200-1350 °C in a nitrogen environment [4]. As a result, the fibers lose 50% of their original weight due to the loss of nitrogen, oxygen, and hydrogen and become over 95% carbon in composition [4]. Graphitization is performed at temperatures greater than 2000 °C however most GDLs are made only at carbonization temperatures [4].

The dry-laid manufacturing process starts with dry laying the PAN fibers into a thin fiber fleece mat through a carding-combing process. In turn, the fibers of the fleece mat are bound into a PAN non-woven mat by a hydroentangling method that involves moving the fleece mat through an array of water streams whose diameters and spacing range from 80-150 μm and 15-50 streams cm^{-1} respectively [4]. The mat is then carbonized at 1000-1500 °C and a carbon or graphite powder with a resin binder can be added if warranted. This is followed by a second carbonization or graphitization process [4].

Inherently, the carbon fibrous material in GDLs is hydrophilic and can absorb and pin water droplets in the GDL pores. Therefore the bulk part of the GDL is treated with polytetrafluoroethylene (PTFE) to increase the GDL's hydrophobicity, or its ability to shed water. On the cathode side of a PEMFC, this is applied so that the GDL can effectively transport water away from the CCL to avoid blocking passageways utilized by the reactant gases to reach the CCL. The anode side GDL is also treated as water is prevalent due to the humidified hydrogen inlet stream. The treatment is especially important under startup conditions where a warm humid stream comes in contact with a cool PEMFC in an automobile chassis and, in turn, condenses [4]. Another reason for this treatment is because the wettability of the untreated carbon used for many GDL substrates can fluctuate due to changes in surface chemistry in an operating PEMFC [4]. PTFE loadings range from 5 to 30 wt% PTFE but excessive PTFE loading hinders electrical conductivity as well as porosity and therefore optimal performance has been shown for those with 15 to 20 wt% PTFE [1,4]. A variety of methods are used for PTFE treatment including brushing, spraying, or dipping [1]. The most common method is dipping the GDL into a PTFE suspension, drying the

coated GDL in an oven, and finally sintering it at 350 °C to ensure that the PTFE is secured to the surface [4].

1.1.3 Microporous Layer

A MPL with pore sizes on the order of 0.1-0.5μm is often added to the catalyst layer facing side of the already PTFE treated bulk fibrous part of the GDL to further manage liquid water that is present in PEMFCs as well as decrease the amount of electrical contact resistance with the catalyst layer [1,3,4]. The most typical MPLs consist of carbon black powder and PTFE to act as a binder [1,4]. PTFE is present in the MPL for two main reasons:

i. Taking the high surface area carbon particles and binding them into a unified layer
ii. Allowing for the layer to become hydrophobic in nature [5]

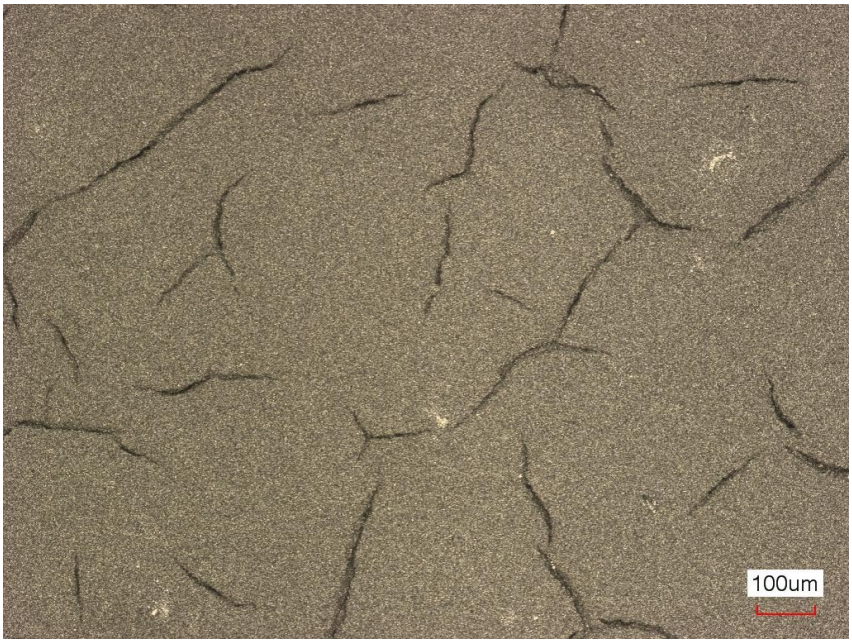

Figure 3: CLSM image of the MPL (SGL Group Sigracet® 25BC).

The presence of a MPL has been shown to increase overall performance by helping to avoid membrane dry out at low current densities and flooding of the GDL and catalyst layer at high current densities [6].

1.2 Characterization of the GDL

The characterization of GDL properties is needed to show the effect of the GDL on PEMFC performance. Different GDLs have inherent properties that can be ideal for different applications and the effective measurement of these properties is essential for the advancement and optimization of future GDLs. The same characterization methodologies used on fresh GDLs can be used for post-degradation analyses as well as for the identification of degradation mechanisms of the GDL. There are various complexities that can arise in measurements as most GDL properties are interrelated and affect each other so careful design and validation is warranted in any of the experiments [1]. Characterization methods include the areas of electron transport, water transport, heat transport, mechanical behavior, porosity, permeability, surface morphology, and surface wettability [1,4–6].

1.2.1 Compression

GDLs need to be compressed to operate properly in a PEMFC. Compression allows for proper sealing as well as an adequate electrical connection. Therefore many GDL properties such as thickness, gas and water permeability, and electrical conductivity are measured under different compressions [1]. Compression also affects the microstructural morphology of the GDL and MPL and therefore close attention must be paid to elastic and plastic deformation [5]. At the point of plastic deformation, the GDL may be subject to premature fracture and if the GDL is too compressible, it may deform into the flow field [1]. There is no standard compression value for PEMFCs as almost all have different geometries and flow field

designs and will most likely use different types of GDLs [1]. GDL compressive properties are characterized by compressing the GDL in between two flat plates and subsequently measuring deflection in the through-plane direction as a function of compressive force [4]. It is also important to ensure that a gasket of proper thickness surrounds the GDL exactly for proper sealing. A PTFE sheet gasket may be used as a hard stop to prevent further GDL compression. These gaskets are designed to compress to different known thicknesses and therefore, if the acceptable range of thicknesses is known for a particular GDL, the proper gasket can be chosen and can act as a safeguard to ensure that the GDL will never get compressed beyond its elastic region.

1.2.2 Porosity

The GDL's most important micro-structural property is its porosity since so many fluids are transported through the GDL at any given time during PEMFC operation [5]. Although a GDL that is highly porous will allow for superior mass transport, it will decrease the overall electrical conductivity of the substrate as well as its compressive properties [5]. A GDL with a MPL added to it will have a lower porosity than just a plain GDL substrate and a higher PTFE loading has the same effect [1]. GDL porosity can be determined through the measurement of the bulk density of the GDL which can be determined from the thickness and areal mass [4]. The average porosity of a GDL substrate is defined as

$$\varepsilon = 1 - \left(\frac{\rho_{b,u}}{\rho_s}\right)\left(\frac{L_u}{L}\right) \tag{4}$$

Where $\rho_{b,u}$, ρ_s, L_u, and L are the GDL bulk density, density of the GDL solid phase, uncompressed thickness, and compressed thickness respectively [4]. The anisotropic fiber structure inherent to the GDL makes it difficult to characterize with respect to porosity. The

porosity of the GDL can also be measured by using mercury porosimetry or the immersion method [1].

1.2.3 Permeability

The permeability of a porous medium is defined as the medium's propensity to transport fluid, regardless of phase, through its pores in the presence of a pressure differential and affects the rate at which the fluid travels through the pores [1,3]. The permeability of a GDL can be measured in both the in-plane and through-plane directions and depends on parameters such as thickness, density, PTFE loading, fiber structure, and the presence of a MPL [1]. Similar to GDL porosity, permeability is also anisotropic due to the random orientation of the fiber structures and, in turn, pore network [5]. Attaining the Darcy coefficient, k, is the simplest form of determining a GDL's permeability and Darcy's Law can be employed

$$Q = \frac{-kA}{\mu}\frac{\Delta P}{L} \tag{5}$$

where Q, A, μ, $\Delta P/L$ are the fluid flow rate, cross-sectional area of flow, viscosity of the fluid, and fluid pressure gradient across a GDL of compressed thickness L [3]. The most common unit of permeability is the Darcy which is equal to 10^{-12} m^2 and typical gas phase permeability values are 5-55 Darcy [3,4].

1.2.4 Electrical Resistivity and Contact Resistance

The GDL's capability to transport electrons through its solid components, or its electrical conductivity, is dependent upon its thickness and the flow field channel width and is quantified by measuring its in-plane and through-plane electrical resistivity [1]. The electrical contact resistance between the GDL and its surrounding components, the CL and flow field,

is also important as electrons must be transferred effectively from the GDL to achieve optimum performance and is dependent on GDL compression [1]. The through-plane electrical resistance, R, is measured in a simple experiment that involves compressing the GDL in between two highly conductive and flat plates of low contact resistance, applying a designated compression to the system, passing a direct current (DC) through the GDL, and subsequently measuring the voltage drop between the two plates [4]. From Ohm's Law,

$$\Delta V = IR \tag{6}$$

the resistance, R, can be calculated as both the current, I, and voltage drop, V, are both known [3]. The added resistance due to the bulk of the flat plate as well as the contact resistance between the plates and the GDL can be neglected if the electrical conductivity of the two plates is high and the contact resistance is low [4]. The through-plane electrical resistivity, ξ, can, in turn, be calculated from obtaining resistance through Equation (7).

$$\xi = R\frac{A}{L} \tag{7}$$

Values have been attained for through-plane in the vicinity of 0.08 Ω cm [4].

1.2.5 Thermal Conductivity

The GDL must conduct heat away from the CCL where the reaction takes place without introducing a large temperature gradient across itself [4]. PTFE loading increases the overall thermal conductivity of the GDL at low compression but has the opposite effect at higher compressions and the presence of a MPL decreases both the contact resistance and thermal conductivity [7]. On the contrary, the humidification of the GDL increases the thermal

conductivity [8]. Typical values for the thermal conductivity of the GDL in the through-plane direction are in the range of 0.2-1.8 W m^{-1} K^{-1} [9].

1.2.6 Wettability

The wettability of a porous medium directly affects how water behaves when adjacent to it and within it. When two or more fluids inhabit a GDL, one fluid tends to be attached more easily to the solid surfaces of the GDL pores and, in turn, displaces the other fluid [3]. The fluid absorbed more strongly on the surface and the displaced fluid are called the wetting and nonwetting fluid respectively. The most prevalent method of measuring surface wettability is the sessile drop method in which a small drop of purified water is dispensed from a syringe onto the surface of the GDL and the contact angle is measured by fitting a tangent to the three-phase point where the liquid surface touches the solid surface [4]. The water droplet size should be no larger than 1 mm in diameter so that the weight of the droplet itself does not affect the contact angle. Also, the angle must be measured before substantial evaporation ensues [4]. A solid surface is completely wetted with a liquid when the contact angle is 0°. The liquid is considered wetting to the solid surface at contact angles below 90° and the solid surface is hydrophilic. The liquid is considered nonwetting to the solid surface at contact angles above 90° and the solid surface is hydrophobic. In hydrophobic PTFE coated GDL pores, water and air are the nonwetting and wetting fluid respectively. The carbon fibers of the GDL are inherently hydrophilic and therefore certain areas of the GDL are hydrophilic and water and air are considered the wetting and nonwetting fluid respectively. The bulk treatment of the GDL with PTFE as well as the addition of a MPL makes the surface hydrophobic in nature. The pore size diameter also has an effect on the hydrophobicity of the

surface [1]. Figure 4 shows a water droplet emerging from a hydrophobic GDL on the right and a water droplet emerging from a hydrophilic GDL on the left.

Figure 4: Water emergence from a GDL with a hydrophobic surface (right) and a hydrophilic surface (left) (Reproduced from [3]).

1.2.7 Surface Morphology

The surface morphology, or form and structure, of both the GDL and MPL can be studied using a scanning electron microscope (SEM), transmission electron microscope, or a CLSM. The effect of structural degradation and morphological changes on both the GDL and MPL can be directly visualized using these tools [1]. Carbon paper GDLs have a higher tortuosity and smoother surfaces than carbon cloth GDLs which has been shown to lead to the stagnation of water droplets at the cathode side of PEMFCs under higher RH conditions [10]. The surface morphology of a GDL changes with compression and the GDL itself can intrude into the flow field channel in an uneven manner due to its non-uniform fiber structure. This leads to both a pressure drop across the flow field channels as well as a non-uniform distribution of reactant gases [11]. The surface of the MPL is smooth and fine in nature due to the fine carbon powder particles that the MPL is comprised of [1]. Some MPLs have

cracks or defects in their surface that are on the order of tens of micrometers in width which may act as preferential pathways for water to travel to the adjacent GDL fiber structure [6].

1.2.8 Compositional Analysis

The arrangement and concentration of elements that a material is comprised of is defined as the material's composition. Material composition can be investigated using an energy dispersive spectroscopic analysis, also called energy dispersive x-ray (EDX) analysis, application which is used in conjunction with a SEM. This method is capable of displaying both the elements that a designated area on the surface of a material is comprised of as well as the concentration of each particular element within the same designated surface area. This tool can be used to identify compositional changes that occur on the surface of the GDL from the degradation tests.

1.3 Water Management in PEMFCs

Water management within PEMFCs is one of the most widely studied topics in PEMFC research as it is critical that a complete understanding of how the water behaves within all the components of a PEMFC, under all operation conditions, in all external environments, and at all points in the lifetime of the PEMFC. With respect to water management research, the GDL is of high interest as it directly affects PEMFC performance. However, the heterogeneity of both the chemical makeup, wettability, and solid structure of the GDL complicates the study and understanding of water transport within it [12,13].

1.3.1 Water Balance in a PEMFC

A balance must be reached in PEMFC operation where a proper membrane hydration level can be maintained to efficiently conduct hydrogen protons without allowing too much liquid

water into the cell [14]. The GDL is the largest contributor to managing the water in a PEMFC [15]. This excessive water can block pathways in the GDL that are needed for the supplied reactant gases to reach the catalyst layer which can result in performance loss and flooding of the cell. At high current densities, the cathode GDL becomes an area of high risk for flooding as water is produced at the adjacent CCL. Flooding is a localized phenomenon and can be caused by one or more of the following [3]:

i. Type of GDL used as well as PTFE loading and presence of a MPL
ii. Flow field channel dimensions
iii. Operating conditions

If one of the above three factors is changed at any point, a flooding condition that is present can be terminated. Therefore, maintaining a water balance is a delicate task where the optimization of all components and operating conditions for the application of the PEMFC is key to avoid flooding [3]. Figure 5 showcases the water transport that can occur at any point and time during operation of the PEMFC. Typically, the inlet gases to both the cathode and anode of the PEMFC are humidified externally before they enter the flow field channels. The two main causes of water flux across the membrane are electro-osmotic drag and back diffusion. Electro-osmotic drag occurs when water molecules present at the ACL are pulled along with the hydrogen protons across the membrane. Back diffusion occurs when water diffuses from the cathode to the anode due to the concentration of water being greater at the CCL than the ACL. Finally, water is always produced at the CCL and must be transported out through the GDL on the cathode side and subsequently the adjacent flow field.

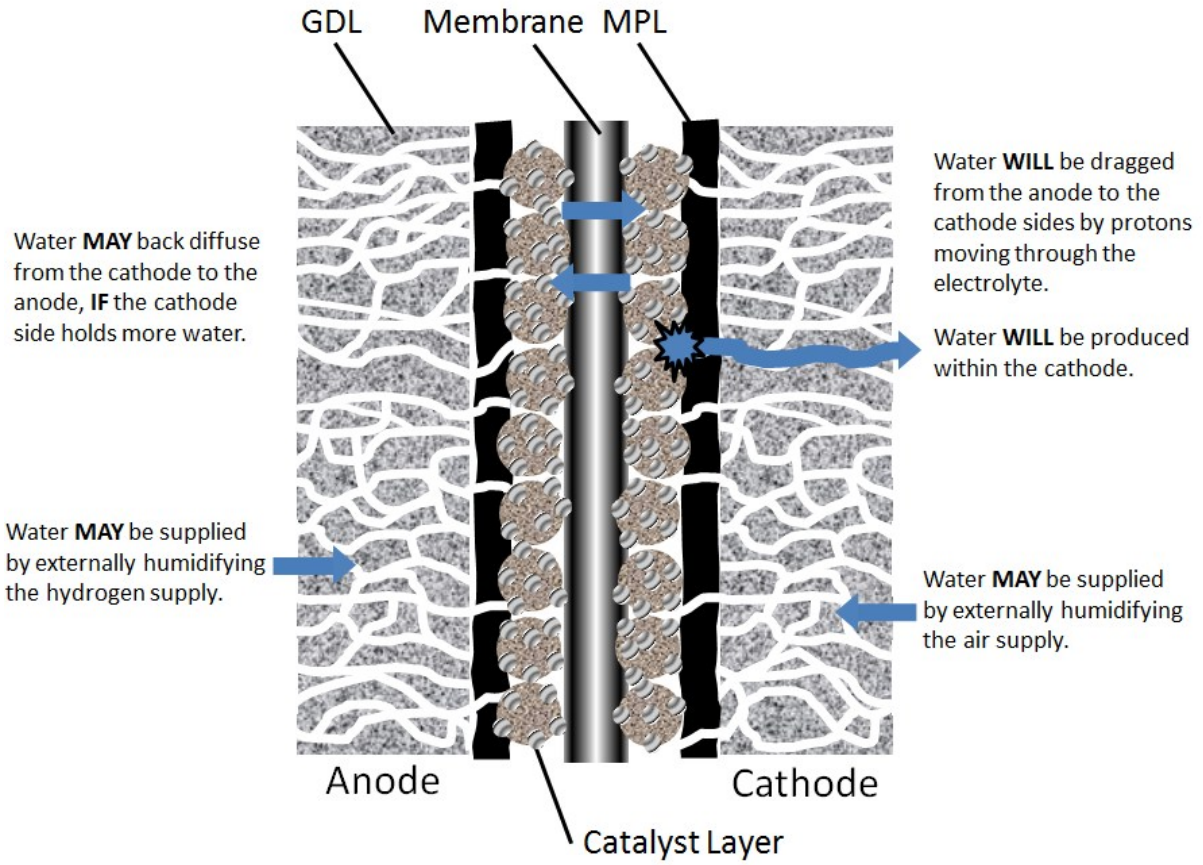

Figure 5: Diagram of water transport phenomena with a PEMFC (Reproduced from [16]).

1.3.2 Water Production at the PEMFC Cathode

The theoretical water production rate, or water mass flow rate, at the PEMFC cathode is a function of the current density, j, produced and can be calculated by applying Faraday's law,

$$\dot{m}_{H_2O} = \frac{jA}{nF} MW_{H_2O} \tag{8}$$

where A, n, F, and MW_{H2O} are the active area of the catalyst layer, equivalent electrons per mole of water produced, charge carried on one equivalent mole, and the molecular weight of water respectively. The latter three are 2 e^- eq mol^{-1}, 96,485 C eq^{-1} and 18.02 g mol^{-1} respectively. The current density, j,

$$j = \frac{I}{A} \tag{9}$$

defines the current produced per unit area of catalyst layer, A. Simply dividing $\dot{m}_{H2O}$ by the density of water, ρ_{H2O}, will give the volumetric flow rate, $\dot{V}$,

$$\dot{V} = \frac{\dot{m}_{H_2O}}{\rho_{H_2O}} \tag{10}$$

of water produced.

1.3.2 Water Transport Mechanisms of the GDL and MPL

During PEMFC operation, immiscible fluid flow, or the simultaneous flow of two or more fluids that are not soluble in each other, occurs within the GDL. This means that inside the GDL, a clear distinction can be made between the fluids as they are separated due to an interfacial tension caused by an imbalance of molecular forces at the line of contact between them [3,17]. Because the rate of water production is very small at the cathode, the viscous forces within the fluid are also small and therefore the main driver of water transport becomes the force caused by capillary pressure, P_c [6]. The capillary number, Ca, and viscosity ratio, M, govern immiscible flow

$$Ca = \frac{u_{nw}\mu_{nw}}{\sigma} \tag{11}$$

$$M = \frac{\mu_{nw}}{\mu_w} \tag{12}$$

where u_{nw} is the velocity of the nonwetting phase, and σ is the surface tension between the wetting and nonwetting fluid. Capillary numbers on the order of 10^{-8} and a viscosity ratio of 17.5 are typically seen under normal PEMFC operation conditions [18]. Capillary pressure driven flow, or capillary action, in a porous medium is caused by the pressure differential

that exists between two or more phases that occupy the given porous medium. The capillary pressure is therefore a metric used to describe the propensity of a porous medium to absorb the wetting phase or resist the nonwetting phase [17]. The Laplace equation for capillary pressure

$$P_c = P_{nw} - P_w = \sigma\left(\frac{1}{r'} + \frac{1}{r''}\right) = \frac{2\sigma}{r^*} \tag{13}$$

is used to quantify the capillary pressure that exists between wetting and nonwetting phases in porous media. As pictured in Figure 6, r' and r'' are the two principal radii of the interface between the surface of a solid pore and the liquid surface curvature.

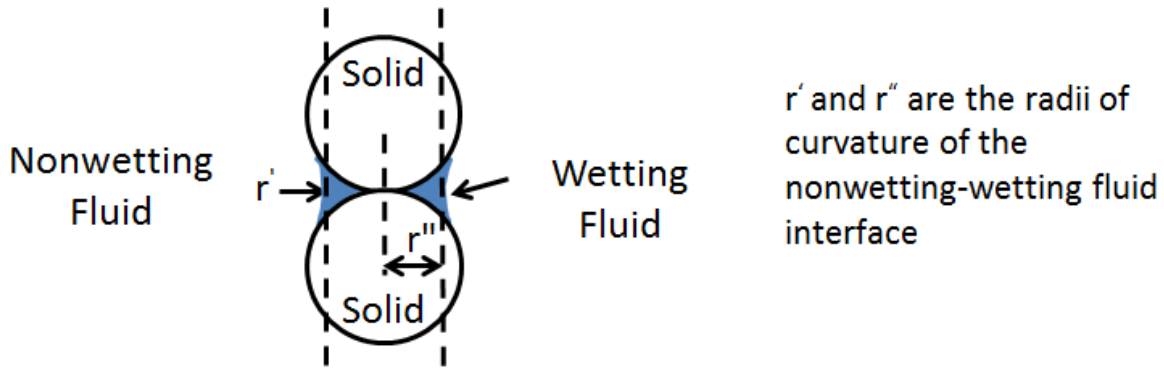

Figure 6: Equilibrium at a curved water/air interface (Reproduced from [17]).

The mean radius of curvature, r^*, is on the same order as the average pore radius of a GDL. The surface tension, σ, for water that is in contact with air can be determined through the following correlation

$$\sigma\ (N\ m^{-1}) = -1.78 \times 10^{-4}(T) + 0.1247 \tag{14}$$

where T is the water temperature in degrees Kelvin [3]. When the average pore radius of a GDL is substituted in for r^* in the Laplace equation, the variable contact angle that results from different PTFE loadings can be added

$$P_c = \frac{2\sigma cos\theta}{r^*} \quad (15)$$

where r^* is taken as a negative value to allow for the signs to match the original Laplace equation [3]. All the terms in the Laplace equation are a statistical average taken over the entire GDL void space of interest [17]. Due to the heterogeneity of the GDL pore structure, a statistical approach using the Laplace equation cannot be applied on a microscopic level throughout the entire GDL surface. Instead, modeling of the GDL is done macroscopically and incorporates parameters inherent to bulk GDL characteristics [3]. It can be inferred from Equations (13) and (15) that capillary pressure increases as pore radius decreases and therefore the capillary pressure of a GDL with a MPL is higher than that of a GDL carbon fiber structure.

The capillary pressure as a function of water saturation is of great importance in GDL water transport studies. Udell et al. [19] developed a semi empirical equation that related capillary pressure to water saturation in a porous medium with hydrophobic or hydrophilic pores.

$$P_c = \sigma cos\theta \left(\frac{\varepsilon}{k}\right)^{\frac{1}{2}} J(s) \quad (16)$$

where,

$$J(s) = 1.417(1-s) - 2.210(1-s)^2 + 1.263(1-s)^3 \; if \; \theta \; < 90° \quad (17)$$

$$J(s) = 1.417s - 2.210s^2 + 1.263s^3 \; if \; \theta \; > 90° \quad (18)$$

J(s) is called the Leverett function and allows for the incorporation of the saturation of liquid water into the capillary pressure equation assuming hydrophobic or hydrophilic pores. However, a GDL pore network is not uniformly hydrophobic or hydrophilic throughout its entire network and therefore a concrete definition of whether the GDL is considered hydrophobic or hydrophilic as a whole is not possible. Therefore, water will act as the wetting fluid in untreated fiber regions and as the nonwetting fluid in areas that are treated

with PTFE. A single function cannot describe this situation but Equations (16), (17), and (18) can be useful in allowing for a basic understanding of the capillary pressure behavior in hydrophobic and hydrophilic pore networks [3].

An understanding of the capillary pressure as a function of both nonwetting fluid saturation, s_{nw}, and wetting fluid saturation, s_w, or

$$P_c = P_c(s_{nw}) \tag{20}$$

and

$$P_c = P_c(s_w) \tag{21}$$

with respect to hydrophobic and hydrophilic pores is important in describing the capillary pressure driven flow through a GDL. The drainage and imbibition curves in Figure 7 show these relationships in a porous medium as well as the effect of hysteresis.

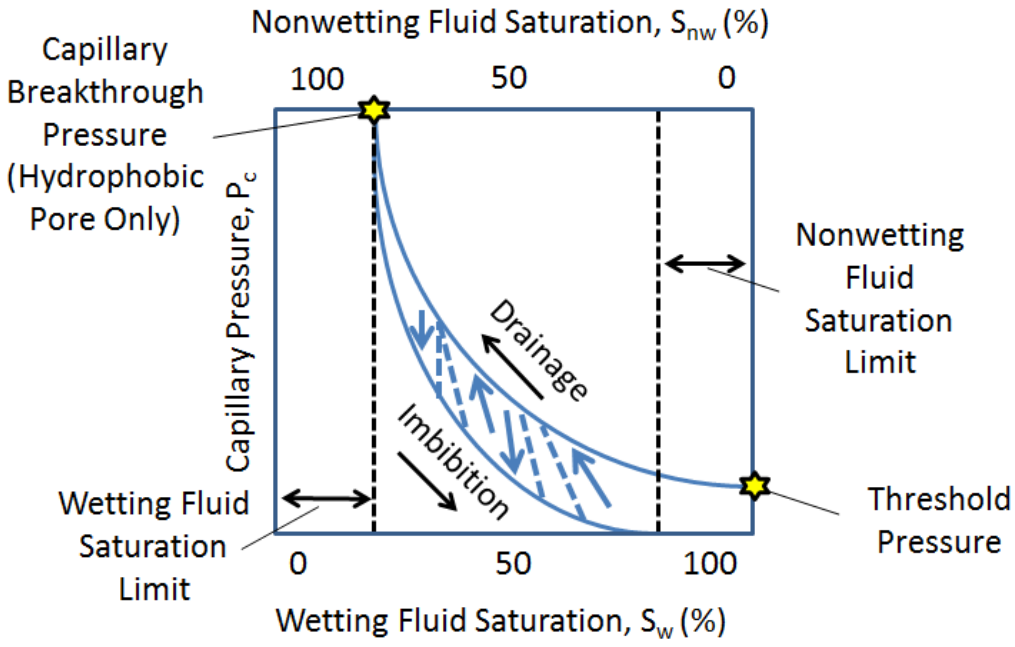

Figure 7: Capillary pressure versus wetting and nonwetting fluid saturation in a porous medium (Reproduced from [17]).

The hysteresis that is inherent to all GDLs causes the capillary pressure curves to differ based on whether the GDL is originally saturated with water or air in hydrophobic or hydrophilic regions [17]. The threshold pressure is the pressure of the nonwetting fluid that must be reached before drainage and displacement of the wetting fluid can be initiated. Capillary pressure rises as the saturation of the nonwetting fluid increases. Eventually a saturation limit is reached to which the capillary pressure cannot increase any further. Imbibition occurs when the nonwetting fluid displaces the wetting fluid. As imbibition occurs, the capillary pressure decreases along with the saturation of the nonwetting fluid. The nonwetting and wetting fluid saturation limits can change as drainage and imbibition reoccur due to the effect of hysteresis. The blue dotted lines and arrows in Figure 7 represent the hysteresis effect.

The GDL is saturated with water non-uniformly as water does not easily move into areas of the GDL under the lands of the flow field while water droplets move easily into the areas under the channels [6]. The flow process in the GDL is heterogeneous and the water will flow through straightest and most column-like pathways [6]. This phenomenon closely follows the discontinuous drainage displacement phenomenon of Haines jump theory [6]. The theory states that as water emerges through a porous network of random sizes, it will breakthrough and then a void below the breakthrough location will form due to a throating effect. This void is signified in the lower portion of Figure 8 as the black dotted line. Water may not travel through this path again but may jump to a different breakthrough point instead. The water transport mechanisms through the MPL are not clearly understood. However it is believed that the MPL restricts the flow of water to only enter the GDL through the surface cracks and other defects that are inherent to the MPL as shown in Figure 9 [6].

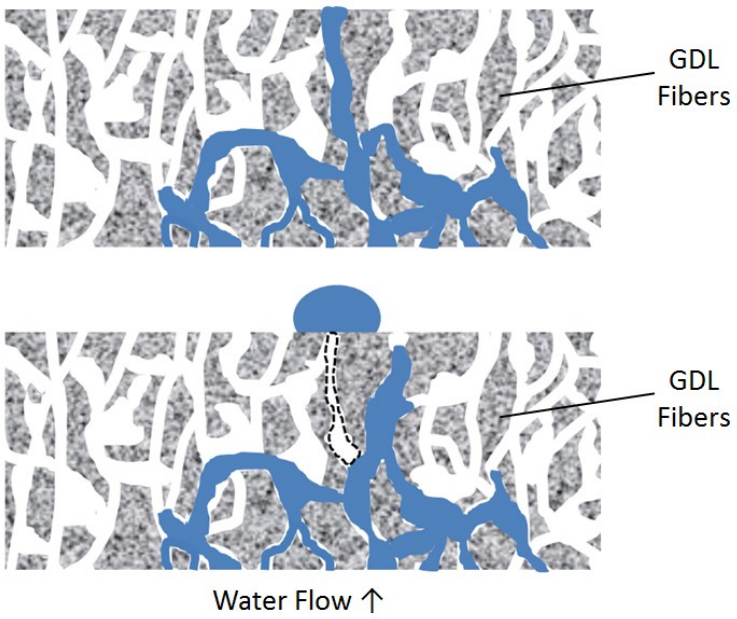

Figure 8: Haines jump discontinuous displacement drainage process. (Reproduced from [6]).

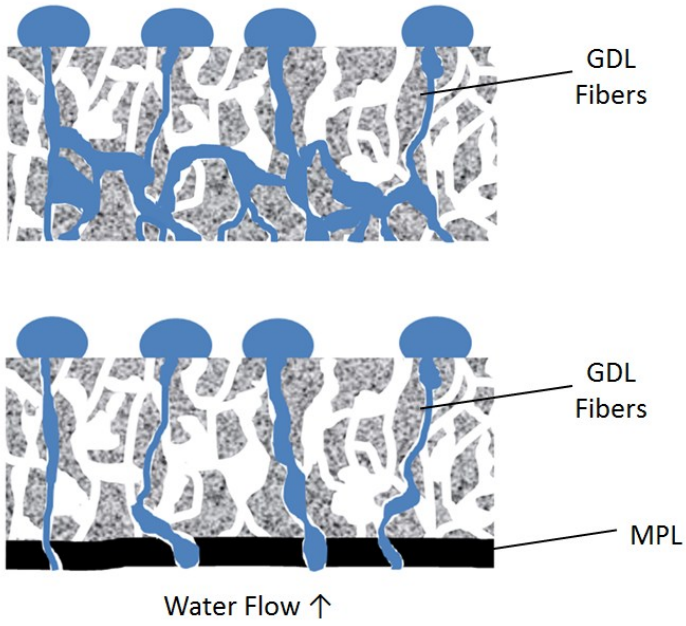

Figure 9: Water drainage of a GDL without a MPL (top) and with a MPL (bottom). (Reproduced from [6]).

The MPL therefore stabilizes the water pathways through the GDL and Haines jumps are not present in GDLs with a MPL due to the fact that the water pathways are not as easily connected in the fiber network [6].

1.4 Electron Transport and Production in PEMFCs

An electric circuit is required for the electrochemical reaction that occurs in PEMFCs as current and ions must flow to complete the reaction. The integrity of the electrical and ionic conductivity of the fuel cell components that make up a PEMFC is essential to maintain performance. Also the electrical and ionic conductivity may fluctuate depending on the operational parameters. High temperatures will decrease the electric conductivity of materials such as graphite and steel due to increased molecular collision frequency and have the opposite effect on the ionic conductivity [3].

The boundary between the open pore for the reactants, the membrane and the catalyst is known as the triple-phase boundary (TPB). Increasing the TPB will increase the reaction site density and, in turn, increase the uniformity of electron and ion conduction through the fuel cell componentry. However, in most PEMFCs, a thin film of electrolyte with a limited permeability to reactant coats the catalyst layers and allows the reaction to occur beneath it unrestricted by TPB locations [3]. The catalyst layer is quite complex as it has to allow an adequate amount of reactant sites, readily conduct electrons and ions, and be porous and thin enough so that it doesn't hinder performance.

1.5 Degradation Tests

The durability and lifetime of PEMFC componentry can be improved through the employment of various types of degradation tests where failure modes, or degradation

mechanisms, of PEMFCs can be identified. In turn, mitigation strategies can be implemented [20]. A fuel cell can be run at steady-state for a lifetime and then the proper assessments may be made. However, these types of tests take much time and are costly to run. In many circumstances, ex situ degradation investigations are performed as they save both time and money. Accelerated stressors that are suspected to affect fuel cell performance can be applied to fuel cells and their components in order to identify performance degradation rates and component damage levels. The investigation of fuel cell performance in in situ applications and component properties in ex situ applications before and after the degradation test is carried out is essential to identifying the degradation mechanisms [20].

1.6 Investigated GDL and Properties

The type of carbon paper GDL used in this study was a Sigracet® SGL 25 BC model that is offered by SGL Group - The Carbon Company. Fresh samples were procured for the ex situ experiment. This type of GDL was chosen because it is commonly used in PEMFC applications. Table 1 outlines the properties of the GDLs given by the manufacturer.

Property	Unit	SGL 25 BC
Thickness	µm	235
Areal Mass	g m^{-2}	86
Porosity	%	80
Air Permeability	cm s^{-1}	1
Through-plane Electrical Resistance	mΩ cm^2	< 12
Substrate PTFE Loading	wt%	5

Table 1: Properties of GDL under investigation.

It features a 30-50μm thick MPL with PTFE impregnation in both the fiber structure and MPL. The MPL on the SGL 25 BC is the manufacturer's standard issue.

2. LITERATURE REVIEW

2.1 Water Management in the GDL

Studying PEMFC components and how they manage water has been a critical area of research due to the fact that maintaining a water balance within the cell is of such great importance. Because the GDL is the component that most directly affects water management within the cell, much experimentation has been carried out. Using these types of experiments can, in turn, help to characterize the degradation of the GDL and how it affects its ability to manage water.

Understanding the capillary pressure driven water transport through the GDL substrate has been a main goal of the fuel cell research community as it is believed to be the main driver of liquid water flow through the GDL. A capillary pressure transport study was recently conducted by Lu et al. [6] in 2010 on a number of fresh GDL samples from different major manufacturers that featured different PFTE loadings and MPL coatings. A specially designed ex situ setup was employed to study GDL samples in a simulated physical PEMFC environment and under select simulated operation conditions. The study was mainly focused on understanding the liquid water breakthrough dynamics across the GDLs through both visualization and CBP measurement. Figure 10 shows a basic schematic of the experimental setup and a three dimensional view of the water chamber. Water was injected through the GDL using a syringe pump that was set at a flow rate equal to the theoretical water production rate seen at the cathode of a PEMFC during operation.

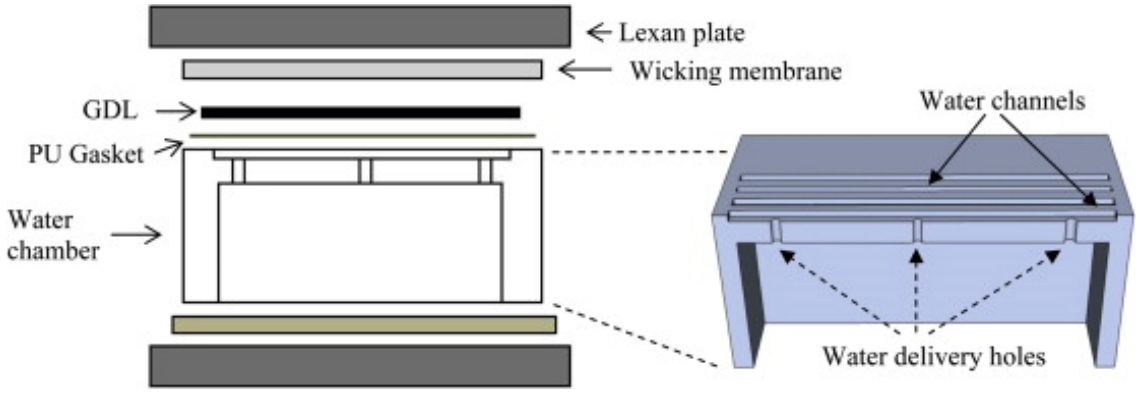

Figure 10: Test setup for the visualization of the water breakthrough dynamics in the GDL [6].

The water flow rate was 10 μL min^{-1} which corresponds to a current density of 1.2 A cm^{-2}. The GDL was located on top of an array of 8 channels each measuring 30 mm long, 0.7 mm wide, and 0.4 mm deep with 0.5 mm lands in between [6]. Much like in a real PEMFC flow field, the channel array was of a weaving type with an 11° angular channel switchback every 5 cm to prevent shear stress in the GDL sample [6]. A water chamber was located below the channels and was connected to them via three water delivery holes per channel. This allowed for an even distribution of water across the GDL sample. For sealing purposes, a polyurethane (PU) film surrounded the periphery of the water delivery channels under the GDL and a PTFE gasket surrounded the GDL sample. A thin wicking membrane was placed on top of the GDL in order to uptake the emerging water away from the GDL to be visualized through an adjacent clear Lexan® plate. A similar Lexan® plate was located on the bottom of the setup and through holes in both plates allowed for them to be fastened together with bolts. In turn, the GDL sample could be compressed to a similar value to what it would see in a PEMFC environment. If the GDL being tested had a MPL, the water was injected through the MPL side first just as it would occur on the cathode side of a PEMFC.

The water was always injected up through the GDL sample. The researchers measured the water pressure with a differential pressure transducer and it was assumed that the air within the GDL pore network was at equilibrium with the air in the surrounding environment. Since the air pressure in the GDL was assumed to be atmospheric and the water flow rate of 10 μL min^{-1} being supplied was low enough to neglect viscous forces, the pressure read by the sensor was a direct measure of the capillary pressure. The results showed that the capillary pressure continuously grew as water entered the GDL until it reached a peak pressure at breakthrough to the other side. This initial water breakthrough pressure peak was designated as the CBP value. Subsequent water breakthroughs were observed as drainage and imbibition occurred in the GDL. This showed that capillary pressure is dynamic during fuel cell operation. Through the use of visualization and the wicking membrane, it was also determined that the water breakthrough location remained the same over repeated water breakthroughs in GDLs with MPLs while the location changed in GDLs without MPLs. They suspected that the MPL therefore allows for the stabilization of preferential water pathways through the GDL main pore network. The CBP, DCP, and the water breakthrough locations for SGL 25 BA and SGL 25 BC GDLs are shown in Figures 11 and 12 respectively. The SGL 25 BC sample featured a MPL while the SGL 25 BA did not. This increased interconnection of water means that more pores in the GDL have water in them and therefore there are fewer pores available for reactants to enter. This means that there could be an increased risk of flooding a cell if a MPL is not present or is degraded. The SGL 25 BC GDL sample exhibited a higher breakthrough pressure value than the SGL 25 BA. The authors attributed this to the smaller pore size of the MPL. The researchers were not able to

accurately quantify the compression value applied to the setup or investigate the same experimental procedures using degraded GDL samples.

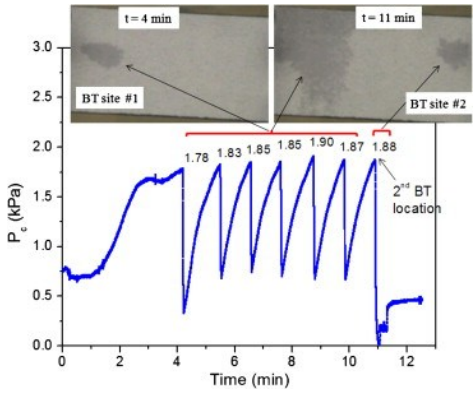

Figure 11: Water breakthrough dynamics through an initially dry SGL 25 BA GDL sample. BT denotes breakthrough and the numbers are the CBP values [6].

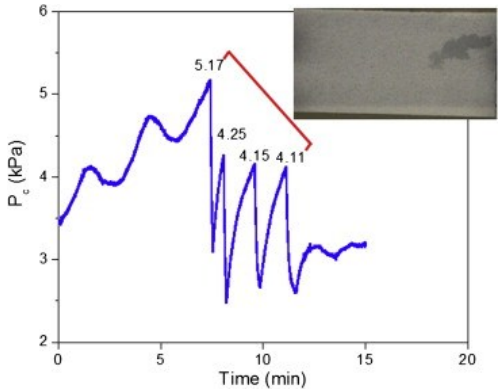

Figure 12: Water breakthrough dynamics through an initially dry SGL 25 BC GDL sample. BT denotes breakthrough and the numbers are the CBP values [6].

Bazylak et al. [21] in 2008 employed fluorescence microscopy to visualize the droplet emergence and detachment from the GDL while also measuring the CBP in an ex situ experiment. The GDL and surrounding silicone rubber gasket were sandwiched in between a Plexiglas® base and a polydimethylsiloxane (PDMS) plate with a 3.7 mm × 4.5 mm channel

[21]. A syringe pump was used to inject liquid water through the bottom of the GDL at a rate of 5 μL min^{-1} to simulate a high current density if it is assumed that there is no water transport between the anode and cathode [21]. An air flow rate of 2 m s^{-1} was passed on the top side of the GDL through the PDMS channel to carry away the water once it broke through the GDL sample [21]. A pressure sensor was placed close to the inlet of the Plexiglas® base to measure the CBP most accurately. It was observed that the water pressure grew until it reached the CBP value where droplet emergence occurred on the surface. At first, droplets emerged and detached causing small and fast pressure peaks. Eventually, the channel became filled with water slugs and water droplets no longer appeared causing the DCP to change to longer, more rolling pressure spikes [21]. It was also observed through the fluorescence microscopy portion of the study that residual liquid water particles were left within the GDL over time and acted as pinning sites for future droplets. Pinning affects droplet emergence frequency and size [21]. The authors also saw the location of water breakthrough change over time due to possible rearrangement of the internal water pathways. They also saw that when a new location formed, water receded from the prior breakthrough location and suggested that water branching occurred within the pore network [21].

A similar study was carried out by Gostick et al. [22] in 2008 as well where capillary pressure was measured as a function of saturation, $P_c(s_{H2O})$, for both water injection and withdrawal. Their method controlled the gas pressure in the GDL sample in order for the capillary pressure values to remain constant. A water reservoir rested on an analytical balance in order to determine how much water was in the GDL at any given time. The test section sandwiched a 19.05 mm diameter GDL sample with a porous hydrophobic membrane and a porous hydrophilic membrane above and below the sample respectively [22]. A top

plate, spring, plug, and compression tube rested on top of the hydrophobic membrane. A liquid distributor with 20 800 μm holes in it distributed the water beneath the hydrophilic membrane and rested in an indented location in the base plate [22]. The hydrophobic membrane acted as an air exit pathway but trapped the water after breakthrough while the hydrophilic membrane acted as an entry for water but not air. With only the hydrophilic membrane fixed on top of the base plate and liquid distributor, a suction of -10 kPa was applied via a liquid port on the base plate to rid the system of water [22]. The rest of the setup was in turn assembled with the spring applying only a slight pressure to the plug so that the GDL sample was not compressed. Air pressure was then applied through a gas port on top of the top plate for a net pressure of -20 kPa across the system. The liquid suction is subsequently turned off and the water reservoir was connected to the liquid port. This setup procedure ensured that no water touched the GDL before capillary pressure measurement. A syringe pump was then connected to the gas port on top to control the air pressure. The air pressure changes effectively changed the capillary pressure and the mass of the water in the reservoir was monitored throughout the experiment so that the amount of water that was present in the GDL could be known. The GDLs tested were a sample of Toray Industries® TGP-H-090 and SGL 10 BA and both samples exhibited a saturation plateau as well as residual saturation after water was injected and withdrawn respectively [22]. It was found that the Toray sample, which lacked rough binder and PTFE, filled up to a saturation of 1 while the SGL 10 BA reached a limiting saturation of 0.84 [22]. No water entered the GDL until positive capillary pressures were reached during injection and the saturation level did not start to decrease until negative capillary pressures were reached during withdrawal. Both samples exhibited hysteresis with respect to $P_c(s_{H2O})$. The research presented does not

investigate the change in $P_c(s_{H2O})$ hysteresis as a function of GDL degradation and also does not provide direct CBP measurement.

An ex situ simulation of the cathode side of a PEMFC was recently carried out for GDL samples with four different morphologies by Liu et al. [23] in 2012. Water emergence through the GDL was visualized and coupled with capillary pressure measurement to analyze the dynamics of water transport through the GDL samples. A syringe pump supplied water to the GDL sample which was sandwiched in between two polycarbonate plates. A 20 mm × 5 mm rectangle was cut into the bottom polycarbonate plate to supply water through the GDL and the upper plate featured a 24 mm × 11 mm visualization rectangle that was open to the atmosphere [23]. A differential pressure sensor measured the difference between the atmospheric pressure and water pressure. The GDLs tested were 30 mm × 15 mm carbon fiber, carbon cloth, carbon cloth with a MPL applied on one side, and carbon cloth with MPLs applied on both sides [23]. The samples were all dried in an oven at 80 °C prior to experimentation to ensure that all moisture was evaporated [23]. The simulated water production rates were 10, 20, and 50 μL min^{-1} and the water was injected up through the MPL, if the specimen featured one, and then through the fibrous part of the GDL [23]. The carbon paper GDL exhibited a linear increase in water pressure until the CBP value was reached. Subsequently, a sharp decrease in pressure occurred and a steady state residual water pressure was established. These residual water pressures increased with increasing flow rate. Similar to Lu et al.'s [6] work, this peak pressure value corresponded to the droplet emergence on the surface of the GDL. It was found that when the flow rate was increased, the slope of the pressure rise prior to breakthrough also increased. However, they found that the CBP decreased with an increasing flow rate. The CBP values for the carbon cloth GDL

were all lower than those achieved for the carbon paper and this phenomenon was attributed to their possibly larger pore size. The pressure increased at a slower rate at first, but later shifted to a steeper slope. This was attributed to the higher flexibility of the carbon cloth. The lowest flow rate showed a sharp decrease after the CBP was reached and droplet emerged, but the pressure fell to a higher value than all of the other GDLs without MPLs and then began to rise again to close to the same CBP value where another droplet emerged from the same pore. The authors attributed this phenomenon to the breaking of the liquid water pathway within the GDL pore network. The cloth GDL with a MPL exhibited DCP and through visualization, eruptive transport phenomena was observed where droplets discharge quickly, or burst, through the fibers. The CBP values were higher than those of the GDLs without a MPL as also reported by Lu et al. [6] The GDL with the double-sided MPL exhibited the highest CBP values out of all of the GDLs but did not exhibit DCP. For all the GDL samples, the CBP was the highest pressure achieved and subsequent pressure was always lower. This suggested that the pressure to overcome the surface energy is much higher than that required to drive the flow. Their CBP values decrease with increasing flow rate for the GDLs without a MPL while the CBP values were independent of flow rate for the GDLs with MPLs. Although the researchers presented valuable results, they did not investigate the changes in CBP and DCP due to degraded GDL samples. They also did not compress the entire GDL sample due to the visualization window being open to the atmosphere rather than being a clear solid window structure to evenly compress the GDL.

2.2 GDL Degradation

With respect to current fuel cell research, GDL degradation studies have only recently began to gain popularity as other main fuel cell components have now been refined. Both ex situ

and in situ experiments and analyses have been carried out. Mainly ex situ research has been conducted due to the added effects from adjoining components such as the catalyst layer and bipolar plate when testing in an in situ environment [24]. Ex situ analyses allow for individual GDL ageing and eliminate the need to run an entire cell just to investigate the GDL portions. Long run times along with the complexity of analysis also add to the reason why not much analysis has been done with in situ degradation studies [24]. Durability, in general, is difficult to quantify and improve mainly because of the large amount of experiments and time it takes to carry them out [25]. Much research with respect to the GDL has pertained to measuring the impact of materials and design on PEMFC performance rather than looking at the degradation properties [26]. Changes in the microstructure and surface characteristics of the GDL, which are mainly due to material loss and pore size distribution shifts, are the main causes of change in the water content level and transport properties of the MEA [20]. Zhang et al. [20] calls for further degradation test methods and characterization techniques to be developed in order to make an improvement in the overall understanding of GDL degradation and aging. This will, in turn, aid in the progress of reducing GDL degradation [20]. The hydrophobicity of a GDL has been shown to decrease after 11,000 hours of operation and also due to cold start conditions [26]. Borup et al. [27] demonstrated that as the temperature increased, so too did the loss of hydrophobicity of the GDL. This also occurred when sparging air was used instead of nitrogen. In conclusion, the GDL degradation was mostly attributed to the MPL. Borup et al. [27] also found that the performance loss of a GDL aged in nitrogen was not as substantial as the performance loss of a GDL that was degraded in air.

Borup et al. [27] also conducted a review of mechanical degradation and reported that few literature papers investigate the effect of compression of gas diffusion layers on the performance of PEMFCs. SGL Group presented a relationship between in-plane electrical resistivity and compression stress of a GDL [15]. A study on the effect of fuel cell compression on GDLs was carried out by adjusting bolt torque for different GDL materials. An optimal bolt torque for GDL materials with MPLs was found. It was also found that for GDLs without a MPL, less torque gives the highest power and that higher torque can cause damage to the GDL [15]. This study provides adequate insight on compression but leaves out the effects of temperature, water flow rates, and current densities.

Lee et al. [24] investigated GDL compressive strain under steady-state and freezing conditions. They found that the highest value of strain that occurred under steady state aging conditions at 80 °C and 200 psi for 1500 hours was 0.98% [24]. When the temperature was increased to 120 °C the strain moved up to 2 % [24]. An investigation where the load was increased also yielded a higher strain value than steady state at 1.5% [24]. Ultimately, the results showed that temperature had a greater effect on maximum strain than load. They also studied the effects of freezing conditions on various GDL properties such as electrical resistivity, bending stiffness, air permeability, surface wettability, porosity, and water vapor diffusion. There was no change in in-plane resistivity, bending stiffness, surface wettability, porosity, and water vapor diffusion throughout the course of 50 consecutive freeze and thaw cycles between -35 and 20 °C [24]. However, an increase in both in-plane and through-plane air permeability was observed at 18% and 80% respectively [24]. This was due to material loss during permeability measurements. The test GDL was a Toray Industries® TGP-H-60 carbon fiber paper GDL with a 6 wt% PTFE loading and 0.6 mg cm^{-2} MPL loading [24]. The

GDL samples were exposed to a temperature of 165 °C and a compression of 2.8 MPa for 2 minutes in a heated press in order to simulate the stresses that are introduced during the MEA manufacturing process [24]. The GDL samples measured 23 mm × 30 mm and were set up in a test fixture that had 0.8 mm channels and 0.55 mm lands [24].

The effect of compression on liquid water transport and microstructure of PEMFC GDLs was studied by Bazylak et al. [28]. The authors found that when the GDL was compressed, preferential pathways form for water transport. Fluorescence microscopy was employed to provide ex situ visualization of liquid water transport through the GDL when placed beneath an optically transparent clamping plate [28]. Transient image data was captured with a CCD camera and indicated that areas of compression in the GDL coincide with preferential pathways for water transport and breakthrough. The fact that preferential flow of water through the smaller pores results from GDL compression contradicts the expected behavior in a hydrophobic membrane. This suggested that a loss of hydrophobicity has occurred. The morphological changes in the GDL under the effect of compression were viewed by a SEM. Images show that the compression of the GDL caused not only a break up of fibers, but also the loss of hydrophobic coating [28].

Kim et al. [29] determined that ice formation caused interfacial delamination between the catalyst layers and GDL after 100 freeze/thaw cycles from -40 to 70°C and increased GDL deformation. Carbon fiber fractures also were observed and, coupled with the deformation of the GDL, increased the electrical resistance. This could lead to an increase in water flooding and, in turn, a reduced lifetime and mass transport losses [29]. Mukundan et al. [30] tested freeze-thaw durability down to -80°C using dry ice. Results of their work indicate that multiple cycles could lead to interfacial delamination and GDL failure [30]. Their results also

indicate that the preparation procedure for the MEA and the type of GDL could have a significant impact on freeze-thaw durability [30]. Zhang et al. [20] reported that long periods or repeated pulses of hydrogen starvation and high potential control should cause even more damage to the anode MPL and the GDL via microstructural and characteristic changes due to the fact that they are carbon based. Also, from a mass loss perspective, high flow rates and hot pressing can also become GDL degradation stressors to obtain useful information about GDL degradation during fuel cell operation [20]. It is quite apparent that through this research, temperature has an effect on GDL degradation and performance. Breakthrough pressure investigation of GDLs that were exposed to high temperatures could produce valuable results for the refinement of future GDLs.

Lin et al. [31] performed a water washing experiment in 2008 where GDL samples with a MPL were clamped between two tubes and degraded by being exposed to an extreme liquid water flow rate of 500 mL min^{-1} for 200 hours [31]. The washing area of the GDL samples was 19.6 cm^2 and total area of the samples was 25 cm^2 [31]. The GDL samples used were a carbon fiber paper GDL with a MPL made with Vulcan XC-72 carbon black powder and a 10% fluorinated ethylene propylene (FEP) and 90% deionized (DI) water solution [31]. High resolution SEM and elemental analysis were performed on the GDL and the through-plane and in-plane electrical resistance, weight, density, and porosity were measured before and after the water washing process. Also, an in situ single cell investigation was performed where polarization curves were generated using both the fresh and degraded 25 cm^2 GDL samples. The researchers showed, through the use of a SEM, that the MPL cracked, broke up, and was subsequently washed into the GDL fiber structure over the course of the 200 hours of water washing. However, they did not monitor the same region of the MPL over time but

rather picked different spots to show this phenomenon. The through-plane resistance was measured in 5 different places with 10 mm round contacts at compressions ranging from 0 to 2.9 MPa [31]. An overall decrease in the in-plane resistance of the samples was found after the water washing process. It was suspected that because the FEP 121A solution used in the MPL was an electrical insulator, its breakup and washing into the GDL fibers made the samples more electrically conductive in the in-plane direction. The through-plane electrical resistances measured before and after washing were found to be relatively the same especially under high compressions because the MPL was washed into the GDL fibers. This was confirmed by the fact that the porosity decreased from 56 to 52 cm^3 cm^{-2} s^{-1} [31]. The average porosity of the fresh samples before the MPL was applied was 77 cm^3 cm^{-2} s^{-1} [31]. Therefore if the MPL had completely been washed away, the porosity should have gone back to this initial value rather than the lower value of 52 cm^3 cm^{-2} s^{-1}. The weight of the GDL samples was reduced by an average of 4.5% due to the washing process [31]. Consequently, the average density of the samples stayed around 1.6 g cm^{-3} because the volume decreased much more than the weight [31]. In the in situ portion of the study, the GDLs were tested in an in situ environment at various points of water washing time. The polarization curves showed a decrease in performance with an increasing degree of water washing time. The conditions were the same for each test and current densities of 654 and 403 mA cm^{-2} were achieved at 0.6 V for the fresh and fully degraded samples respectively [31]. The researchers concluded that the loss of MPL was the main factor in this performance loss.

Chen et al. [25] looked at the electrochemical durability of the GDL under simulated PEMFC conditions. In this ex situ method, the electrochemical oxidation of the GDL was investigated after potentiostatic treatments for up to 96 hours at potentials ranging from 1 to 1.4 V in 0.5

mol L^{-1} of H_2SO_4 [25]. Morphology, resistance, gas permeability, and contact angle measurements were taken before and after oxidation. It was found that the maximum power densities of the fuel cells when held at 1.2 and 1.4 V for 96 hours decreased by 178 and 486 mW cm^{-2} respectively [25]. Corrosion at a high potential allowed for electrochemical impedance spectra to show a significant change in the ohmic resistance, charge-transfer resistance, and mass-transfer resistance of the fuel cell.

Wu et al. [26] reported that GDL oxidative and electro-oxidative stability were improved by using graphitized fibers during the preparation of the GDL. Graphitized corrosion resistant carbons in MPLs could reduce carbon loss due to corrosion as well [15]. Owejan et al. [32] found a 25% improvement in the start/stop degradation rate at 1.2 A cm^{-2} from employing Pureblack® graphitized carbon material in the MPL. Kim et al. [29] discovered that pressure uniformity of the GDL onto the catalyst layer was found to be a key parameter to allow for the mitigation of freeze-induced physical damage. They determined that more stiff GDLs allow for a more uniform compression under the channels and lands of the flow field which can, in turn, mitigate surface cracks. When more flexible cloth GDL samples were tested, they were subject to severe catalyst layer surface damage. GDL thickness as well as the presence of a MPL were investigated and were not observed to have any major contribution toward the mitigation of freeze damage when the catalyst layer was in contact with liquid [29].

In this study, wettability is characterized by measuring surface contact angle. Gurau et al. [33] studied the degradation of GDLs by estimating the changes in wettability along with the changes in absolute permeability due to carbon corrosion and carbon surface oxidation. Wettability was measured by looking at the internal contact angle to water and surface

energy of a solid matrix. Results showed a reduction of the solid matrix hydrophobicity due to the surface oxidation of carbon. The surface energy of the solid matrix increased while the internal contact angle to water decreased. Five samples were tested in an ex situ experiment where aging at 2 V for 10 minutes and 2 V for 1000 minutes were carried out [33]. Through-plane viscous and inertial permeability measurements were made and increased with carbon corrosion [33].

Aoki et al. [34] quantitatively analyzed the influence of PEMFC cathode degradation on electrode polarization. GDL samples with the catalyst layer applied to them were corroded in an ex situ simulation and changes in catalyst layer surface area, wettability, and pore volume were determined after the simulation. Polarization curves were generated and analyzed before and after a long term operation and the influence of the degradation of the GDL and catalyst layer were evaluated. It was found that the catalyst layer corroded much more than the GDL. This corrosion not only affected the diffusion loss of the catalyst layer but also the GDL as well. They found that the increase in GDL diffusion loss was caused by the diffusion loss in the catalyst layer [34].

With respect to solely in situ GDL degradation experiments, Wu et al. [35] studied the degradation behavior of a 6 wt% PTFE content, 190μm thick, commercial Toray Industries® TGP-H-060 carbon fiber paper GDL with MPL when exposed to an array of elevated temperatures and elevated flow rate conditions [35]. Nafion/MPL/polymide anode and cathode GDL isolation barriers were added in order to avoid the possibility of having the catalyst layer affect the GDL during degradation testing. These barriers were added due to the adhesive property of PTFE and carbon particles. The GDL samples were subjected to steady, high temperatures and flow rates for 200 hours [35]. Humidified hydrogen and air

were heated to 120 °C and the flow rates for the hydrogen and air were 7.88 and 31.0 SLPM respectively [35]. These flow rates correspond to a stoichiometry of 7.5 and 11.8 at the anode and cathode respectively and a current density of 1 A cm^{-2}. The stack was tightened down to a pressure of 0.7 MPa [35]. The changes in the GDL's properties over time were characterized by looking at various properties such as through-plane electrical resistivity, porosity, and RH sensitivity. Single-cell performance curves were also generated. The three different sets of GDLs that were aged consisted of unstressed, hot press stressed, and assembly stressed GDLs. All of these properties were investigated before and after the degradation processes. The through-plane electrical resistivity was measured by compressing a 2 cm^2 round GDL sample between two gold plated copper plates to 1.2 MPa, passing a current of 4 A through it with a DC power supply, and subsequently measuring the voltage drop with a multimeter. Decreases in both electrical resistivity and hydrophobicity were achieved. The decrease in electrical resistivity was most likely due to material loss in the fresh GDL samples. Structural weakening could have caused even more material loss in the hot pressed and assembly stressed GDL samples specifically. Polarization curves were generated from running the samples in a single cell setup and show that the ohmic and mass transport losses were greater in the cells tested with degraded GDLs. The ohmic losses were due to the drop off of contact resistances at the GDL/catalyst layer and GDL/plate interfaces due to the non-electrically conductive PTFE loss of degraded GDLs during the performance experiments. The optimal humidification temperatures dropped noticeably when aged samples were compared to fresh ones. This temperature is that at which the fuel cell achieves maximum performance and is a measure of RH sensitivity. The RH sensitivity differences are related to the hydrophobicity changes from before and after the degradation process.

After the degradation process, the assembly stressed sample showed the most hydrophobicity loss and the unstressed GDL sample showed the least. The decrease in optimal humidification temperature for aged GDLs parallels a loss in water management ability. With respect to porosity, a small increase was observed over all the samples and can be due to material loss during the degradation process. The main material lost could have been PTFE and it was concluded from porosity tests that the hot pressing and assembling of GDLs caused accelerated degradation and also weakened the structure. They indicate that further work is needed to measure and distinguish quantitatively the material loss from the substrate and MPL, respectively.

Lim et al. [36] investigated the effect of different GDLs on freeze/thaw condition durability in PEMFCs. The GDL's ability to mechanically support the MEA and its effect on fuel cell performance and durability was studied as well. They tested carbon paper, felt, and cloth GDLs all having MPLs and a 5 wt% PTFE content [36]. They all were similar with respect to porosity and electrical resistivity as well. However, the thicknesses and bending stiffness differed. The range of freeze/thaw temperatures was from -30 to 70 °C [36]. The reactant gases were at a RH of 80%, hydrogen and air utilization were set at 75% and 50% respectively, and the tests were operated at atmospheric temperature [36]. A SEM was used to characterize the surface of the MEAs. Bending stiffness tests were performed on 3.8 cm × 7 cm samples at a bend angle of 15° [36]. Performance characteristics were measured via polarization curves from running the GDLs in single cell setups. The optimum GDL was determined through the correlation of the durability with bending stiffness. The felt GDL showed no change in performance while the cloth and paper GDLs showed significant performance losses. From these tests it was found that sufficient mechanical supporting force

between the interfaces of materials enhances PEMFC durability in sub-zero temperature conditions. The electrochemical surface area and hydrogen crossover current were measured and there was no major change in all three GDLs with respect to both properties. The ohmic or contact resistance and charge transfer resistances were obtained by measuring the alternating current impedance for a single cell. With respect to the ohmic resistance, the paper and cloth GDLs exhibited a much more substantial increase when compared with the felt GDL. This is believable as the ohmic resistance is a measure of the contact resistance which is directly proportional to how poorly the contact is made at the interfaces between the materials. However with respect to the charge transfer resistances, all three types of GDLs exhibited no significant change. The performance decrease observed on the polarization curves could be related to the increase in ohmic resistance. Surface morphologies showed that the catalyst layer with the felt GDL only had small cracks while the other two catalyst layers with carbon paper and cloth GDLs were much more destroyed. The bending stiffness was 185 and 13 times higher than that of the cloth and paper GDLs respectively [36]. This indicates that the felt GDL is less susceptible to expanding and contracting under freeze/thaw cycles and is thus less susceptible to degradation due to its better overall freeze/thaw durability. The catalyst layer morphology investigation also showed that the catalyst layers degraded much more in the areas backed by channels than in the areas backed by lands with respect to the paper and cloth GDLs. The felt GDL had the highest bending stiffness and therefore this phenomenon was least present in its respective catalyst layer. Overall, the most durable GDL was the felt followed by the cloth and paper GDLs respectively.

Few studies quantitatively correlate performance loss with changes in surface properties and the resulting changes in transport properties [15]. Schulze et al. [37] found that the

decomposition of PTFE in the electrodes caused a performance loss that was approximately twice that of the agglomeration of platinum catalyst after 1000 hours of fuel cell operation. The degradation mechanism of the PTFE was not thoroughly discussed however, so the degradation could have been due to the GDL or the catalyst layer [37]. In another study, they found that because PTFE decomposition results in a critical water imbalance and partial loss of electrochemical performance, it can be determined by x-ray photoelectron spectroscopy [38]. In a fuel cell degradation review, Borup et al. [15] stated that changes to the microstructure and surface characteristics of GDLs can cause changes in the water-content levels and transport properties of GDLs. Although some literature supports this idea, there is still little information about the rate at which wettability changes or which key properties that determine a composite contact angle are most susceptible to degradation. They call for thorough studies of how liquid water enters pores whose hydrophobicity has been degraded to various degrees. This information is necessary for the design of GDL materials that can successfully resist this type of degradation [15]. Porosimetry measurements can indicate that carbon is lost from the MPL during lifetime tests. Mercury and water porosimetry measurements have indicated that GDL pore structure changes during lifetime tests. Large pore volume decreases due to compression of the cell while small pore volume increases [15].

Cho et al. [39] recently performed an analysis of the transient response of a PEMFC using degraded gas diffusion layers in 2011. The transient response of the fuel cell is very important as, in automotive applications, there are fast electrical load changes and the cell must respond in a quick manner. The samples used in the experiment featured a MPL and were a commercial type of 325 μm thickness [39]. They had a porosity of 80% and featured a

5 wt% PTFE loading for both the GDL fiber section and the MPL [39]. The samples were degraded by a leaching test using an unspecified solution and their property changes were investigated at 0, 168, 336, 720, 1440, and 2160 hours of leaching using SEM and surface contact angle measurement [39]. A 25 cm^2 in situ cell was employed to show the effect of the GDL degradation on the transient response due to an electric load change of 15 A to 30 A, or 0.6 to 1.2 A cm^{-2}, and then from 30 A back to 15 A under starved, standard, and high saturation operation conditions [39]. The surface contact angle was measured on both the MPL side and the fiber side and the results showed a decrease of about 5 degrees in the surface contact angles on both sides and therefore a decrease in the surface hydrophobicity. SEM images showed that carbonized resins within the GDL fiber network were washed out in spots which left the hydrophilic carbon fillers open to the air. The loss of carbon material in the MPL was found as well as a smoothening of the MPL surface. The in situ portion of the study showed that a voltage loss occurred when the current was changed from 15 A to 30 A at 100% RH and a low air flow rate on a cell using the degraded GDLs and hardly no voltage loss occurred at a high air flow rate. This was because the damaged MPL inhibited the mass transport ability of the GDL sample which is necessary when operating at low flow rates and high RH conditions. At 50% RH conditions, the same trend occurred with respect to voltage loss except for at the excess condition where the voltage loss increased again. This was because of the high mass transport to the catalyst layer from adequate convection and diffusion through the GDL [32]. When the load changes to a higher current density, the membrane becomes dehydrated and, in turn, the resistance within the membrane increased and caused a voltage drop. Eventually the membrane became hydrated again from the humidified gases, electro-osmotic drag, and back diffusion and the voltage was regained

[39]. Their results all indicate a hindrance in mass transport from the decrease in capillary pressure caused by the loss of hydrophobicity in the GDL. The authors believed that the increased fluctuations in voltage with increasing current density were due to an uneven distribution of capillary pressure that would correspond to uneven mass transport through the GDL. They believe the water got stuck and subsequently flooded the GDL in local regions of low capillary pressure. This, in turn, caused unstable membrane hydration and oxygen starvation at the cathode which directly relates to the unstable voltage response observed [39]. Low RH conditions cause the membrane to be dried out due to the water being trapped in the GDL as well. The results from changing the load from 30 A to 15 A also pointed toward hydrophobicity loss of the GDL. Because the flow rates of the reactant gases were held constant over the load change, the low load condition became an excess flow condition and left the membrane highly saturated. The voltage response was higher for the degraded GDL because water remained inside the GDL longer before achieving steady state and kept the membrane hydrated [39]. The authors call for studies on how the hydrophobicity changes in the GDL as well as how changes in its structure affect the mass transport in fuel cells. The authors did not measure the CBP to validate that the loss of hydrophobicity caused a loss of capillary pressure driving force.

Dhanushkodi et al. [40] investigated the degradation and diagnostic analysis of GDLs under humidity cycling. Physico-chemical characterization of the GDL and operational analyses were carried out by using a 50 cm^2 active area membrane [40]. Polarization curves were plotted and utilized to access the effects of wet and dry cycling on GDL performance. The cell was operated for 440 hours and was later removed from the MEA by acid leaching. Gas controlled porosimetry and SEM were employed and showed significant changes in the

surface morphology of both the fresh and degraded GDLs. The hydrophobicity was measured by using thermo-gravimetric analysis (TGA) and electrochemical impedance spectroscopy. TGA showed a 50% weight reduction of PTFE content in the degraded GDL compared to the fresh GDL [40]. They also report that the electrical conductivity of the aged GDL was less than the fresh GDL. However, no operation condition, GDL type, MPL coating, or thickness was reported [40].

In a review of accelerated stress tests, Atiyeh et al. [41] reported that SEM was used to identify substantial changes in the microstructure of the GDL's PTFE particles after prolonged operation. This proves that surface morphology investigation can also contribute to learning more about GDL degradation.

2.3 Research Needs

It is quite evident that, although many GDL degradation studies have been carried out, literature lacks a study that investigates the effect of GDL degradation on capillary pressure driven water transport. Also, there are no water breakthrough studies that use flow field specific materials such as gold plated copper for the channel array. Many of the capillary pressure measurement studies do not accurately quantify a PEMFC specific compression value during capillary pressure measurement as well. Intensive CLSM microscopy studies will add further insight to surface morphology changes due to degradation. In literature, the methods of ex situ degradation have not employed excess water flow through the GDL for extended periods of time at rates seen at the upper limit of PEMFC operation. Also, an ex situ experimental setup that is capable of degrading GDL samples with simulated water flow, electric current flow, compression, and temperature simultaneously is completely novel.

2.4 Objectives

1. Develop a test section that degrades GDL samples via temperature, accelerated water flow, current flow, and compression.
2. Measure the CBP values and observe the DCP as a function of GDL degradation.
3. Measure the surface wettability of both the MPL and fiber sides of the GDL samples before and after degradation.
4. Perform an intensive surface morphology study using CLSM on the MPL and fiber sides of the GDL samples before and after degradation.
5. Perform compositional analyses on MPL and fiber sides of the GDL samples before and after degradation using SEM and EDX.

3. EXPERIMENTAL SETUP

3.1 Design

The experimental setup was designed to expose GDL samples to select conditions seen at the cathode of a PEMFC. These conditions included:

i. typical current density

ii. accelerated liquid water transport (flow rate)

iii. typical compression

iv. typical operation temperature.

Figure 13 shows a detailed schematic of the experimental setup and the various circuits that are required to simulate the PEMFC environment and acquire load and water pressure data.

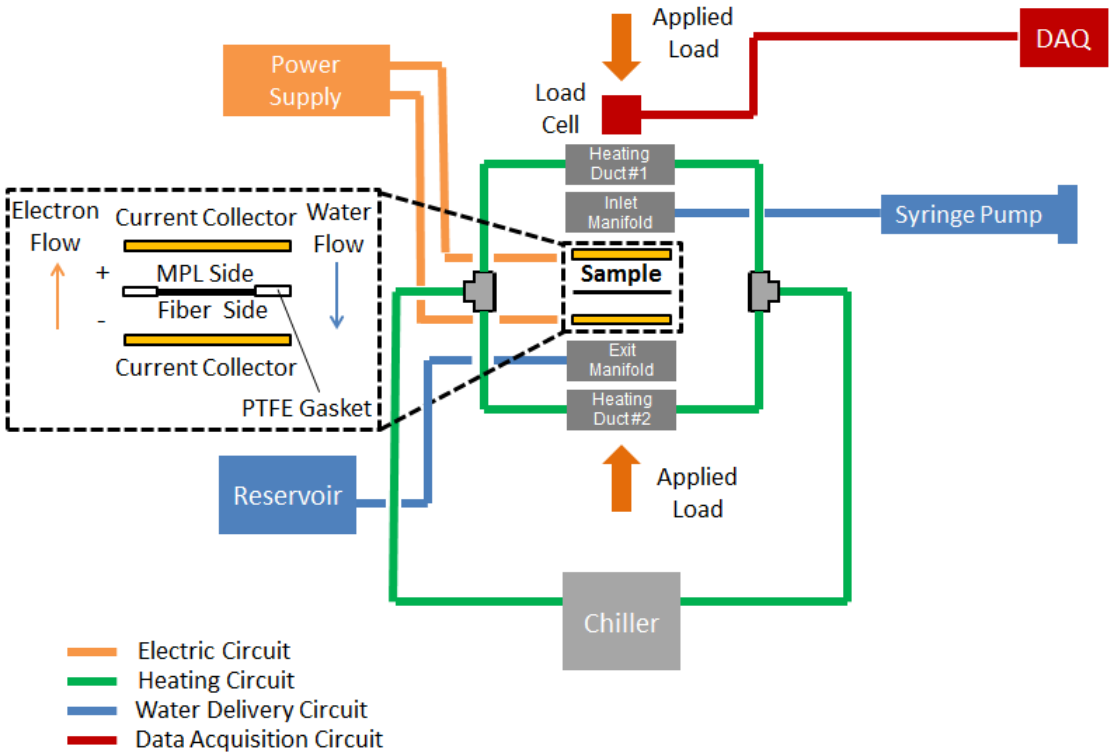

Figure 13: Schematic of the experimental setup.

It can be seen that the water and DC electric current both flow through the GDL sample in the same manner as in a PEMFC. The heating ducts, manifolds, and current collector plates (CCPs) are collectively termed as the test section. This test section accepts a 29 mm × 29 mm GDL sample.

3.1.1 Electric Current Delivery System

The GDL sample is compressed in between two 1 mm thick current collector plates (CCPs). Figure 14 shows the CCPs used which are made of copper and were plated with a 1.3 μm layer of gold to prevent corrosion. The CCPs also feature a 7 channel array of 1 mm wide through channels and 1 mm wide lands. The channels measure 15 mm in length and the array is 13 mm wide for a total active area and water delivery area of 1.95 cm^2 and 1.05 cm^2 respectively. The through channels and lands evenly distribute the liquid water and DC electric current respectively through the GDL during the degradation process. A Hewlett Packard® 6572A DC power supply with a 0-20 V and 0-100 A range was used to pass current through the GDL using 12 AWG 3.3 mm^2 wires. Tabs were cut on one side of each CCP so that the electrical leads from the power supply could be securely connected.

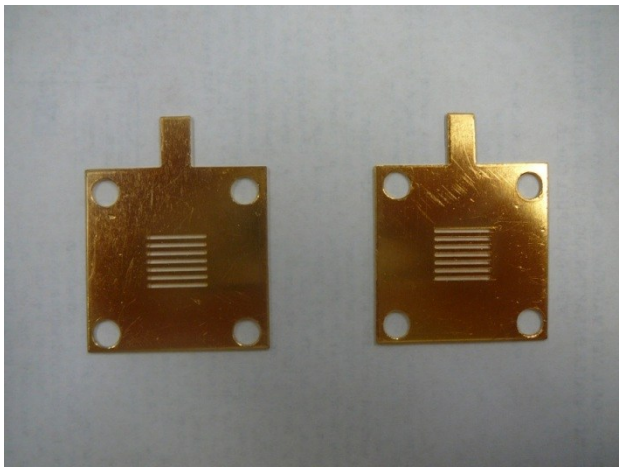

Figure 14: CCPs used in the study.

3.1.2 Water Delivery and Removal System

The CCPs are sandwiched between two 23 mm thick aluminum manifolds whose main purpose is to transport water to and from the CCPs and, in turn, the GDL sample. The inlet manifold is located on top of the CCPs and GDL sample. DI water is delivered to the inlet manifold by a Harvard Apparatus 11 Plus syringe pump outfitted with a 60 mL syringe. A short and level 6.4 mm diameter rubber tube connects the syringe to a fitting that steps down to a 3.2 mm diameter stainless steel tube. Next in line is the differential pressure transducer. Another 3.2 mm diameter stainless steel tube connects the differential pressure transducer to the inlet manifold via a NPT fitting. The water fills a reservoir inside the inlet manifold which then feeds to distribution channels. The inlet and exit manifold reservoirs and channel arrays are identical and one is pictured in Figure 15.

Figure 15: Inlet/exit manifold channel array.

The reservoir is pictured on the left of Figure 15 and the channel array is on the right. The reservoir is 8 mm deep, 4.8 mm wide, and 27 mm long. The reservoir feeds an array of 5 channels and 4 lands that measure 3.2 mm and 2.8 mm in width respectively. Great care was taken in machining the manifolds as they had to be flat enough to seal against the adjacent

CCPs. Because of this requirement, the CCP facing side of the channel arrays were surface ground after they were machined with an end mill. The exit manifold is located below the CCPs and the GDL sample. Water exits the manifolds via a NPT fitting and a 3.2 mm diameter tube that leads to a collection reservoir that is open to the atmosphere.

Both the degradation tests and CBP measurement tests used DI water to pass through the GDL samples. The DI water was dispensed from a Millipore Direct-Q®3 water system and had a resistance of 18.2 MΩ at 23.1 °C.

3.1.3 Heating System

The opposite side of each manifold channel array features a similar channel array that is used for heating the setup. This heating channel array measures 27 mm × 27 mm and the 5 channels are 8 mm deep. This is pictured on the right in Figure 16.

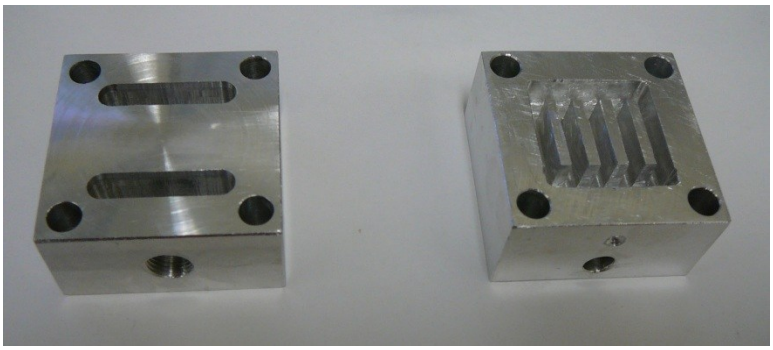

Figure 16: Opposite side of inlet/exit manifold (right) and bottom side of the heating duct (left).

As pictured on the left in Figure 16, the bottom side of the heating duct features two rectangular ports that align with the open areas of the heating channel array to form a pathway for water to flow in and out. A VWR™ International 1196D chiller was employed to supply hot distilled water to the aluminum heating ducts and heating channel arrays.

3.1.4 Compression System

The CCPs, inlet and exit manifolds, and two heating ducts all have four 6.35 mm diameter through holes drilled in them to accept alignment pins. The alignment pins had to be electrically insulating and also needed to withstand high temperatures. Ultra high temperature G-7 Garolite rods were chosen and were turned on a lathe to fit smoothly in the test section through holes and, in turn, align all the components to ensure that they would not shift during the compression process. The top heating duct features a circular indentation machined in the middle on the opposite side to allow for a cylindrical load cell to be inserted securely for load measurement. A screw type clamp held securely by a ring stand was used to apply the designated loads to the system once it was assembled and a liquid and air bubble type level was used to ensure that the system was completely level before any testing was conducted.

3.1.5 Air Purge System

An air purge system was implemented to dry the GDL samples before CBP measurements were made. A tube from a compressed cylinder of ultra zero grade air was connected to an Omega Engineering® FMA-1620A flowmeter which could then be connected to the inlet manifold to purge the manifolds and GDL sample for 30 minutes at 1 L min^{-1}. The air had less than 2 parts per million water content present when bottled.

3.1.5 System Gasketing, Sealing, and Insulation

The interface between the heating ducts and the manifolds was sealed using Permatex® Red High-Temp RTV Silicone Gasket Maker. The CCP and manifold interface was sealed with a specially cut 254 µm thick PTFE sheet gasket that had a thin bead of Permatex® Black Silicone Adhesive Sealant applied on each side. The PTFE gasket acted as an electrical insulator for the CCP and the adhesive sealant was applied for further air and water leakage

mitigation. The GDL was sealed using a 178 µm thick PTFE gasket cut slightly larger than the GDL sample size. The GDL was compressed approximately 57 µm during degradation and CBP measurement. The entire test section was insulated to prevent heat loss when being heated.

3.1.6 Data Acquisition

National Instruments LabVIEW™ programming was employed for data acquisition and the data was imported into a National Instruments LabVIEW™ program at 100 Hz. Figure 17 shows the LabVIEW™ program user interface.

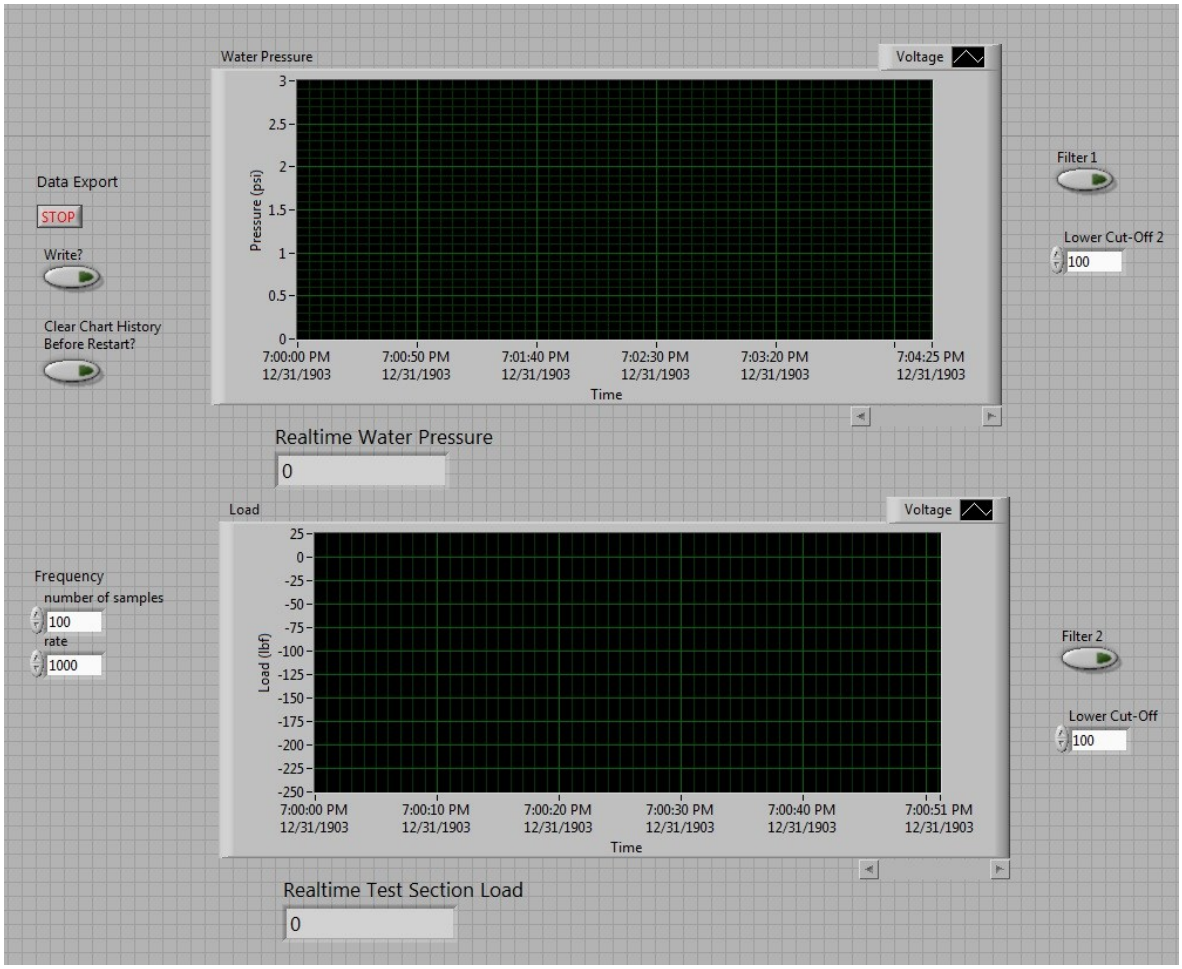

Figure 17: LabVIEW™ program user interface.

The water pressure was measured with a Honeywell® FDW 060-G763-08 differential pressure transducer with a 0-13.8 kPa range and a precision of ± 0.25 % over the full scale output. The compression was measured through the use of an Omega Engineering® LC304-1K load cell with a 0-4.45 kN range and a precision of ± 0.5 % over the full scale output. An Electro Industries DIGI 35A DC power supply was used to provide 10 V of excitation to the both the load cell and pressure sensor. The load cell voltage response was read into a National Instruments 9205 DAQ card in a National Instruments cDAQ-9172 DAQ chassis and the pressure sensor voltage response was read into a National Instruments USB-6008 DAQ card. The program has the ability to write the data acquired to a file which can, in turn, be imported into data analysis and graphing software. Electric current and temperature were controlled and monitored using the interfaces on the Hewlett Packard® 6572A power supply and VWR™ International 1196D chiller respectively.

4. TESTING

4.1 GDL Degradation

Three SGL 25 BC GDL samples were degraded according to the test matrix outlined in Table 2. The water flow rate of 36.4 µL min^{-1} corresponds to the water production rate at a current density of 2 A cm^{-2}.

Sample	Volumetric Water Flow Rate (µL min^{-1})	Test Section Temperature (°C)	Current Density (A cm^{-2})	Compression (kN)	Time (hrs)
S1	36.4	80	0	2.7	75
S2	36.4	23	2	2.7	500
S3	36.4	23	2	2.7	500

Table 2: GDL Degradation Test Matrix.

4.2 Pre and Post Degradation Analyses

Four different property characterization tests were carried out on the GDL samples before and after the GDL degradation process. These tests included:

i. CBP measurement and DCP observation
ii. surface wettability measurement
iii. surface morphology investigation
iv. compositional analysis

Table 3 outlines which of the 4 analyses were performed on specific samples. Only surface morphology studies and CBP measurements were conducted on the S1 sample as it was heavily corroded. The compositional analysis was specifically performed on the S3 sample as material that formed on the MPL surface needed to be identified.

Sample	CBP Measurement and DCP Observation	MPL and GDL Fiber Surface Contact Angle Measurement	Surface Morphology Investigation	Compositional Analysis
S1	Y	N	Y	N
S2	Y	Y	Y	N
S3	Y	Y	Y	Y

Table 3: Pre and post degradation analysis matrix.

4.2.1 CBP Measurement and DCP Observation

The general procedure for CBP measurement consisted of connecting the syringe pump to the differential pressure sensor and, in turn, to one of the manifold entry fittings on the test section. During the test, the DI water made its way from the syringe and through the differential pressure sensor. Then it built up against the GDL in the test section and subsequently broke through to the other side of the GDL sample.

A number of different syringes were investigated for use during the CBP measurements. The 60 mL Medallion® syringe was suspected to be faulty and a validation test was conducted using two 60 mL Medallion® syringes, a 30 mL Medallion®, and a generic 60 mL syringe. The validation setup consisted of connecting the syringe pump to the differential pressure sensor and connecting a needle valve on the end of the pressure sensor. The needle valve was closed off and the syringe pump was started until the water pressure started to rise. Figures 18, 19, and 20 show the pressure rise for the 60 mL Medallion® syringe, 30 mL Medallion® syringe, and the generic syringe respectively. It was found that both 60 mL Medallion® syringes caused unwanted pressure surges due to the plunger seal sticking on the body of the syringe as the water was dispensed. Even when the needle valve was slightly opened, the

pressure spikes still existed. In turn, this affects the CBP measurement as well as the DCP. The plunger seal design for both the 30 mL Medallion® and the generic syringe allowed for a linear water pressure rise with the generic syringe being the most linear. Therefore the generic syringe was chosen to be used during CBP measurements.

When measuring the CBP, it was desired to use a volumetric water flow rate that corresponded to a current density of 2 A cm^{-2}. Therefore the assumed water production area, or active area of simulated catalyst layer, of the CCP was that of the through channels in the CCP which is equal to 1.05 cm^2. Employing Equations (8), (9), and (10) and assuming the density of water as 1000 kg m^{-3} gives a volumetric flow rate of 11.8 µL min^{-1}. However, using this flow rate took excessively long to fill the manifold and CCP before reaching the GDL sample.

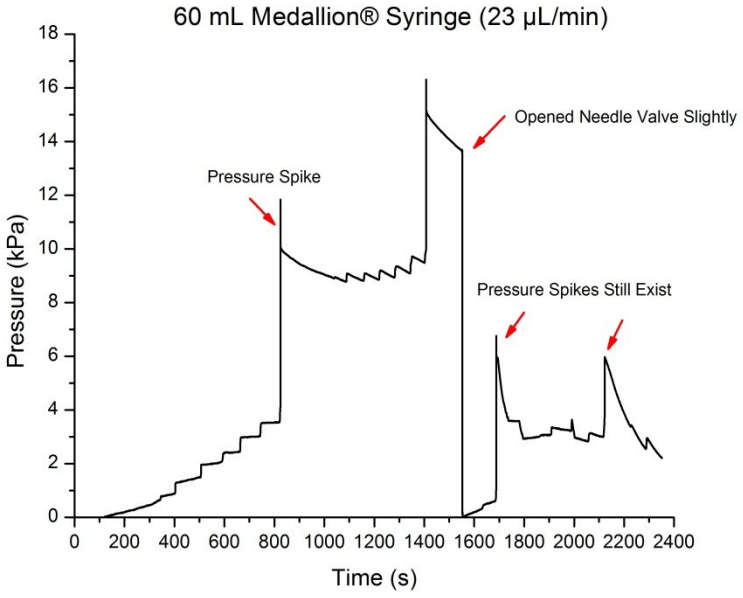

Figure 18: Pressure rise validation for 60 mL Medallion® syringe.

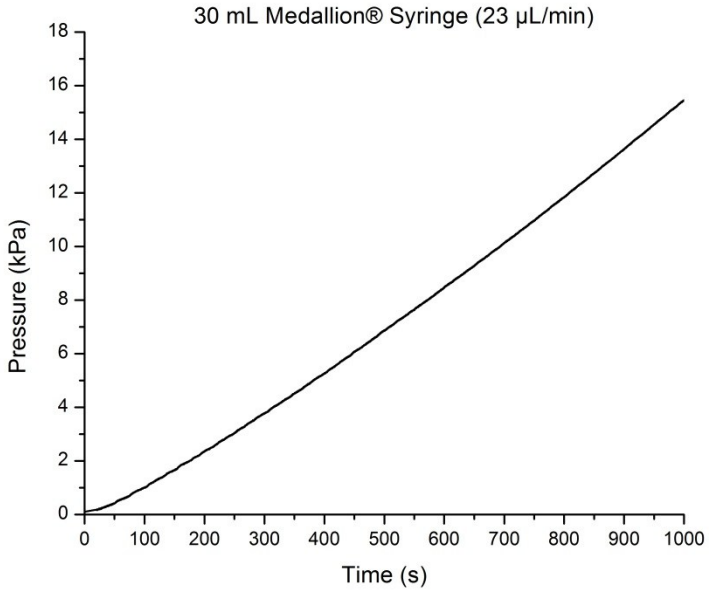

Figure 19: Pressure rise validation for 30 mL Medallion® syringe.

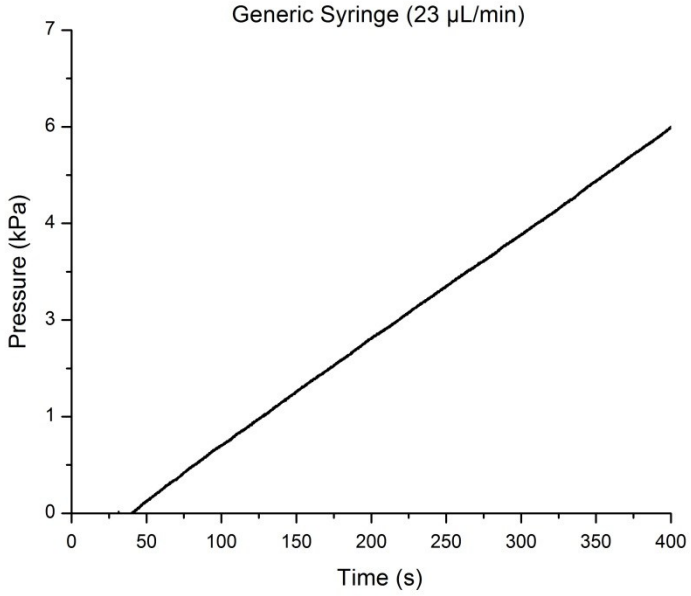

Figure 20: Pressure rise validation for generic syringe.

Therefore, a larger flow rate of 23 μL min^{-1} was chosen and it was determined through the use of Equation (11) that the capillary number was 6.4×10^{-8} for this particular flow rate which is still within the range to produce capillary flow without the added viscous effects. This value was calculated assuming that μ_{H2O} is 1.01×10^{-3} Ns m^{-2}, σ is 0.072 N m^{-1}, and finally that the GDL porosity is 80%. Thus 80% of 1.05 cm^2, the total water delivery area, was used for *A* in Equation (11).

After the proper syringe and water flow rate were chosen, a test matrix was designed to validate the test section and GDL sample orientation as well as the water flow direction for the CBP measurement process. A wicking membrane was also considered to be utilized during CBP measurement for water management purposes and was also integrated into the validation test matrix. This matrix is outlined in Table 4. The water flow rate during these tests was set to 23 μL min^{-1}, the GDL sample compression was set to 4.9 MPa, and the MPL side of the GDL sample, when used, was always facing the opposite direction of the water flow just as it would in an in situ environment. Also, the wicking membrane was always placed adjacent to the fiber side of the GDL sample to effectively remove water after it broke through the GDL sample. TC1 and TC7 were found to produce the most repeatable results with respect to CBP values. TC1 involved pumping water down through the GDL, much like in Figure 13, but only with the addition of the wicking membrane placed adjacent to the fiber side of the GDL sample. However, a schematic of the arrangement used in TC7 is shown in Figure 21. The TC7 configuration was chosen so that the water present in the pathway from the syringe pump to the GDL sample remained completely connected during CBP measurement.

Test Case #	Wicking Membrane	Flow Direction ↑	Flow Direction ↓	GDL
TC1	X		X	X
TC2	X		X	
TC3			X	X
TC4			X	
TC5		X		
TC6	X	X		
TC7	X	X		X
TC8		X		X

Table 4: CBP measurement validation test matrix.

It was suspected that for TC1 the water slugs could disconnect when flowing down through the inlet manifold and CCP. Should this disconnection occur, the disconnected body of water could be transported through the GDL sample by capillary action undetected by the differential pressure sensor. Because it is disconnected from the water that is present downstream in the differential pressure sensor, the sensor will not be able to read an accurate CBP value due to the air gap that would form. Instead, the test section was oriented so that water could slowly be accumulated underneath the GDL by being pumped in through the exit manifold and bottom CCP as pictured in Figure 21. The water eventually is transported up through the GDL sample and the capillary pressure was monitored throughout the entire water accumulation, subsequent breakthrough, and DCP processes with the differential pressure sensor.

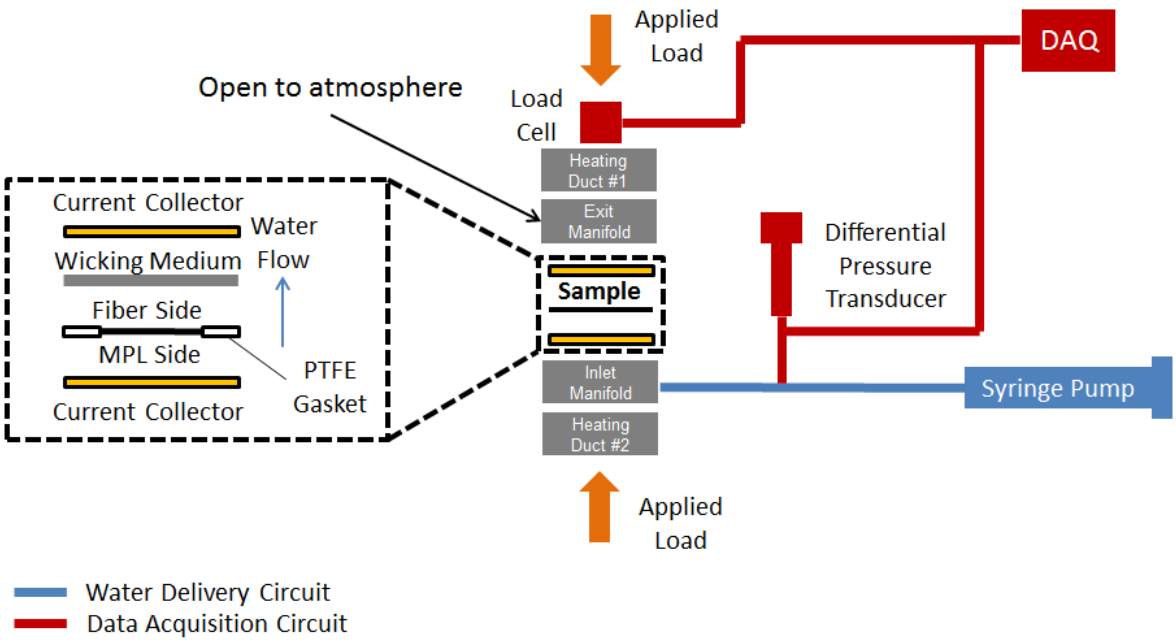

Figure 21: Schematic of the experimental setup for CBP measurement.

As it states in Figure 21, the exit manifold was left open to the atmosphere and therefore the air pressure within the GDL can be assumed to be atmospheric pressure. If the air is assumed to be the wetting fluid and the pressure is atmospheric, Equation (13) states that the water pressure measured by the differential pressure sensor is directly a measure of the capillary pressure. The wicking membrane used was a 0.7 mm thick Porex X-4588 model and was oriented on top of the GDL sample in order to prevent the water from pooling on top of the GDL sample or re-entering it and, in turn, affecting the CBP and DCP. It is comprised of a hydrophilic high-density polyethylene material with a pore size of 80-120 μm [6]. The wicking membrane has a negative capillary pressure and therefore has a negligible effect on the capillary pressure measured [6]. This was verified by TC2 and TC6 where water was pumped through the test section with just the wicking membrane present. No pressure fluctuations occurred during these tests or during TC4 and TC5. Pressure fluctuations occurred only during TC1, TC3, TC7, and TC8. All of these test cases had the GDL sample

present in the test section. Because of this, it was concluded that the capillary transport mechanism inherent to the GDL sample was the sole cause of the pressure fluctuations. Before each CBP measurement, the compression on the test section and, in turn, the GDL sample was set to 4.9 MPa. The load was monitored and adjusted accordingly until the test section exhibited a constant load value so that the test section gaskets could settle and, in turn, maintain a constant load on the GDL sample throughout the CBP measurement process. All the CBP measurement tests were performed three times each and the average CBP value was determined along with the standard deviation.

4.2.2 Surface Wettability Measurement

The static, advancing, and receding contact angles were measured on both the MPL and fiber surface using the sessile drop method before and after being exposed to the degradation test. The static, advancing, and receding contact angles were measured in three different locations for each sample. The contact angles obtained were then averaged. A static contact angle time study was also conducted where a 9 µL DI water droplet was dispensed onto the designated GDL sample surface and monitored over the course of 45 minutes. Although the water droplet size was reduced due to evaporation during the time study, the rate of evaporation was the same in all cases and clear distinctions could still be made with respect to surface wettability over time. An AST Products, Inc. VCA Optima XE contact angle measurement system and software package was utilized to make these measurements.

4.2.3 Surface Morphology Investigation

The surface morphology of the GDL sample fiber structure as well as the MPL surface and surface cracks were investigated intensely before and after being exposed to the degradation test. A Keyence VK-9710 CLSM was used to produce all the images in this work. The

microscope stage did not have a coordinate system and exact images of specific locations on the GDL samples were desired before and after being exposed to the degradation test. A coordinate system was defined by cutting the edge of the GDL sample and defining the cut corner as the origin and then defining positive *X* and *Y* directions as pictured in Figure 22.

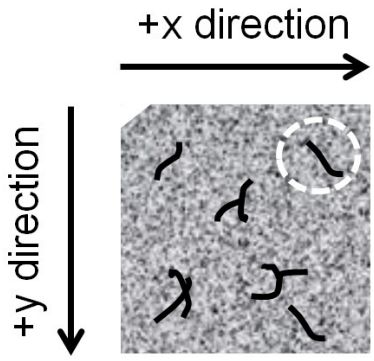

Figure 22: Coordinate system defined for specifying locations under CLSM.

A fine scale ruler was used to carefully measure the distance to a designated GDL fiber structure region or MPL surface crack before and after the GDL sample was exposed to the degradation test. The coordinates were recorded so that the exact same location could be imaged after the degradation test.

4.2.4 Compositional Analysis

A compositional analysis was performed on the MPL surface of the S3 GDL sample. A LEO EVO 50 SEM equipped with an Oxford Instruments INCAx-sight EDX system was employed for this analysis. The degraded S3 sample was imaged as well as a fresh sample that was cut from the same original GDL sheet for comparison. The samples had to be perfectly dry before imaging and were softly clamped with clips onto the SEM stage as to avoid structural damage.

5. RESULTS AND DISCUSSION

5.1 CBP Measurement and DCP Observation

The CBP values obtained for the fresh sample and the degraded S1, S2, and S3 samples are listed in Table 5. Figure 23 shows the water breakthrough behavior over time during the first CBP measurement on the fresh sample. The random capillary pressure spikes confirm a heterogeneous flow pattern as predicted. Water filled the inlet manifold and CCP channels underneath the GDL sample until the water level reached the GDL at the 0 minute point in Figure 23. The water pressure then began to rise linearly as more and more water built up against the GDL. The blue shaded region in Figure 23 marks this time period and the pressure rise is similar to what was seen in Figure 20 where the pump was working against a closed valve. It was first suspected that this pressure rise was caused by the entrance of water into the hydrophobic pore network where capillary pressure would rise with the increase in water saturation as the pores fill according to Equations (16) and (18). However if it is assumed that the GDL was compressed to the thickness of the PTFE gasket surrounding it in the test section, or 178 μm, and the porosity of the GDL is 80%, it would only take approximately 5 minutes for the entire pore volume of the GDL sample to fill up with water at the 23 μL min^{-1} water flow rate used. The linear pressure rise was approximately 13 minutes long and therefore was not caused by water entrance into a hydrophobic region of the GDL but rather a gradual buildup of water pressure against the GDL sample before breakthrough. The start of the red shaded region in Figure 23 marks the point where the threshold pressure was met and where the water first entered the GDL pore network. The pressure continued to rise after water entered the GDL which suggests that the water may have made its way into a hydrophobic area. The transition point from the red region to the

green region could be a CBP value and the green region could be an imbibition curve where air comes into the hydrophobic pores after water breakthrough. However, the time span of the red region is approximately 5.5 minutes. Given the area of the CCP water delivery channels, it would only take approximately 52 seconds to fill all of the GDL pores that were available directly adjacent to the water delivery channels. Even if the entire area of the CCP water delivery channel and land array is considered, the time only increases to about 1.6 minutes. This is still much less time than the 5.5 minutes shown in the red region and therefore the aforementioned claim cannot be made. Furthermore the time span of the green region is 5 minutes which is in stark contrast with the vertical drop in pressure after water breakthrough seen by Lu et al. [6] and the quick 1 minute drop offs seen by Liu et al. [23].

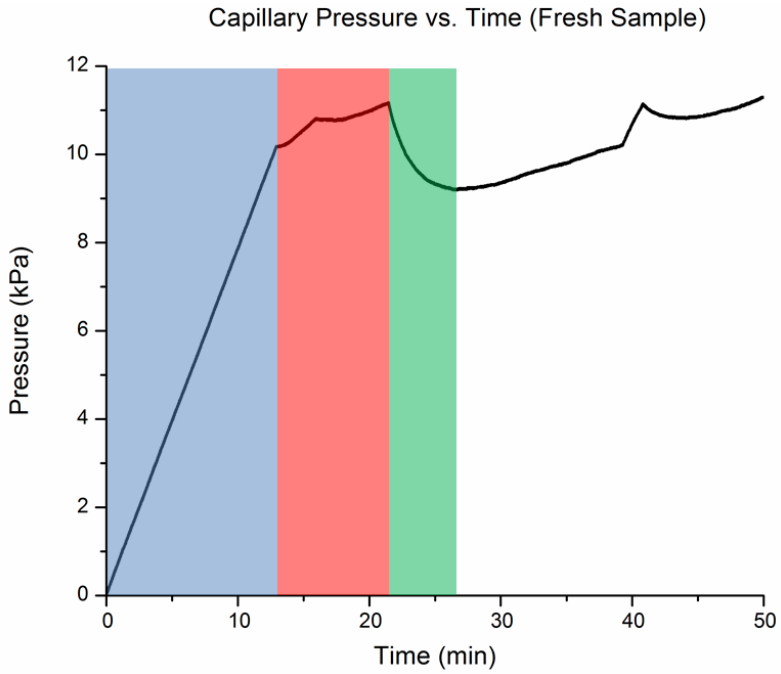

Figure 23: Water breakthrough behavior in the fresh GDL sample (1st test).

Therefore, the DCP after water breakthrough is disregarded as, without visualization techniques, it is impossible to claim what phenomena occurred. Assuming that water enters

into a larger 30 μm diameter cylindrical pore, it would take approximately 0.3 ms for water to fill the pore and break through to the other side of the GDL sample at the 23 μL min^{-1} flow rate used. Therefore, the threshold pressure may be considered the CBP value in this case as water almost instantaneously travels through a single GDL pore once it enters it and all the CBP values reported are also the threshold pressure values.

Figure 24 shows the water breakthrough behavior during the second CBP measurement test. Water broke through and the pressure decreased immediately after which further supports the assumption that the threshold pressure is equal to the CBP value. The third test exhibited similar results as the first two.

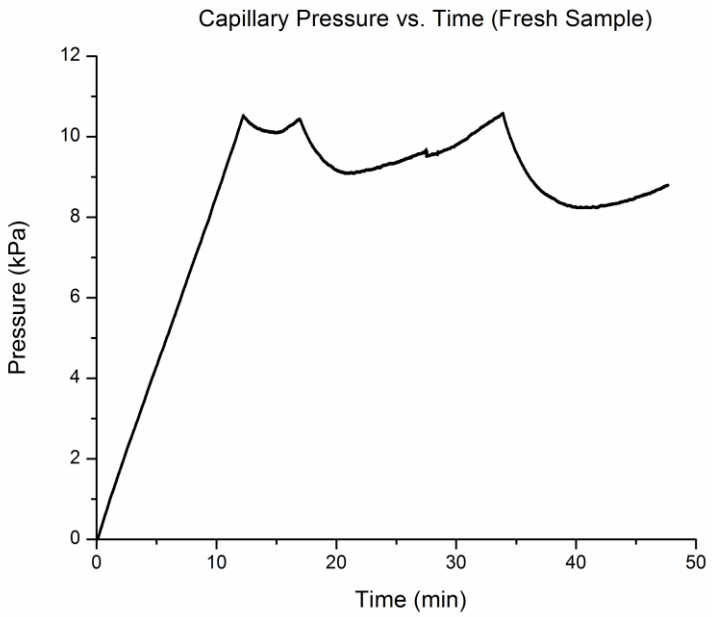

Figure 24: Water breakthrough behavior in the fresh GDL sample (2nd test).

Figure 25 shows the water breakthrough behavior through the degraded S1 GDL sample. It exhibits the same flow characteristics as the fresh sample tests but had a significantly lower

CBP value and the magnitude of subsequent pressure peaks was lower. This suggests that it is easier for water to penetrate the GDL. The other two tests exhibited similar characteristics.

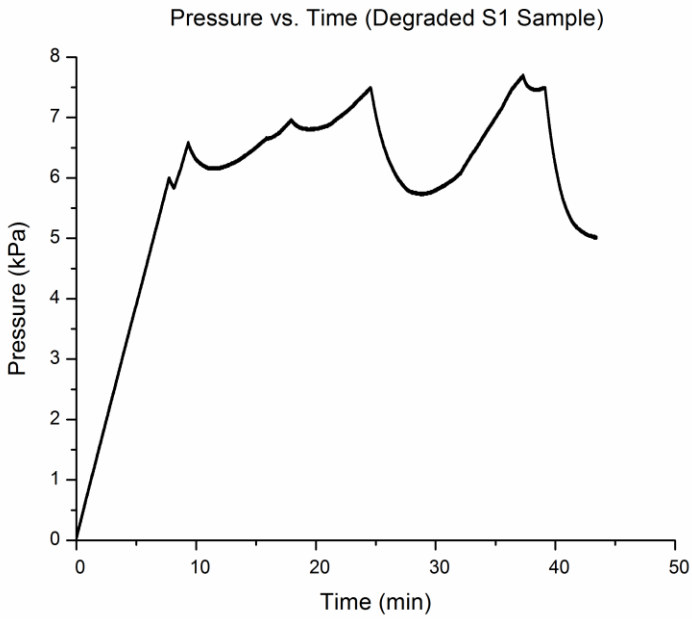

Figure 25: Water breakthrough behavior in the degraded S1 GDL sample (1st test).

The S2 sample exhibited a unique phenomenon shown in Figure 26 where the pressure dropped off after entering the GDL. This is similar to what Liu et al. [23] saw in many of their tests. They attributed this phenomenon to the water remaining connected within the GDL pore network after breakthrough. The second test showed a similar phenomenon but the third test exhibited the same phenomenon seen in the fresh sample tests where DCP occurred after breakthrough.

All of the S3 sample CBP measurement tests exhibited similar characteristics to the first two tests of the S2 sample much like the results shown in Figure 26 where DCP did not occur. Again, this decrease in threshold pressure and CBP suggests a decrease in the hydrophobicity of regions within the GDL as a result of the degradation test.

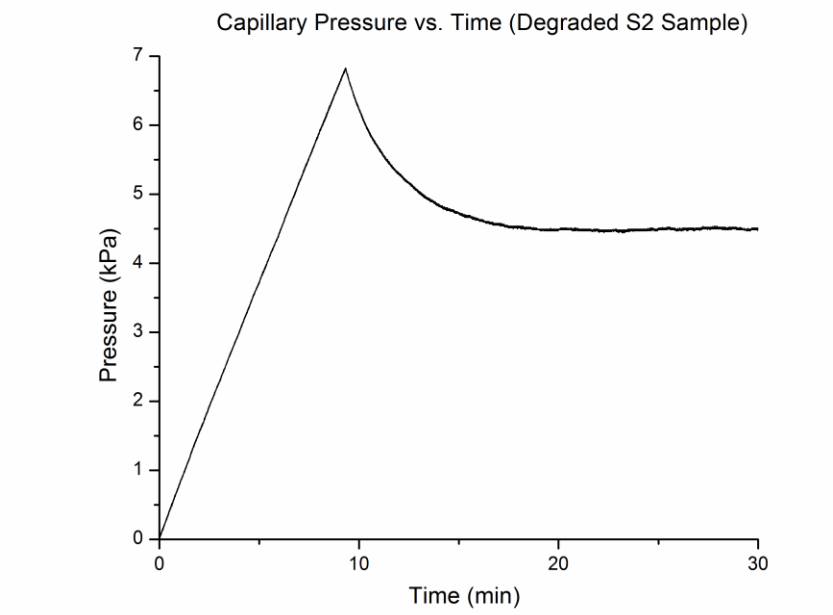

Figure 26: Water breakthrough behavior in the degraded S2 GDL sample (1st test).

GDL Sample	Fresh P_c (kPa)	Degraded P_c (kPa)
S1	10.9 ± 0.4	6.6 ± 0.8
S2		6.3 ± 0.8
S3		8.4 ± 0.2

Table 5: CBP values obtained for fresh and degraded GDL samples.

It can be seen from Table 5 that the average CBP values obtained using the degraded GDL samples were all lower than the CBP values obtained for the fresh GDL sample.

5.2 Surface Wettability Measurement

The S2 sample was the first sample that a surface wettability study was carried out on. A fresh sample cut from the same GDL sheet was used for comparison to the already degraded

S2 sample. Tables 6 and 7 show the average contact angles measured on the surface of the fiber side and MPL side of the GDL samples respectively.

Specimen	Static	Advancing	Receding
Fresh	146	144	144
Degraded	135°	138°	131°

Table 6: Fresh GDL fiber surface advancing, receding, and static contact angle study.

Specimen	Static	Advancing	Receding
Fresh	147°	145°	144°
Degraded	140°	142°	137°

Table 7: S2 sample degraded MPL surface advancing, receding, and static contact angle study.

The static contact angle time studies for the S2 sample fresh and degraded GDL fiber surface and MPL surface are pictured in Figures 27 and 28 respectively. Table 8 and 9 show the contact angles measured for the S2 sample fresh and degraded GDL fiber surface and MPL surface during the time study.

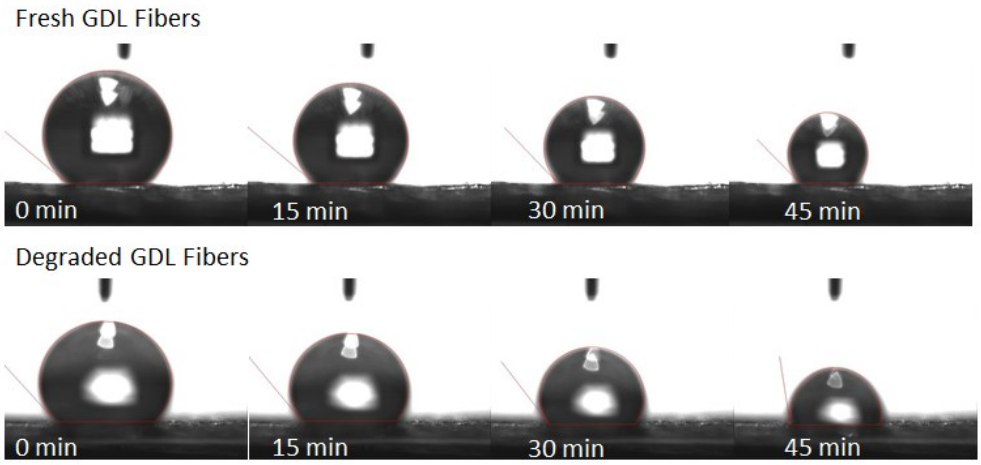

Figure 27: Static contact angle time study for fresh and degraded S2 sample GDL fibers.

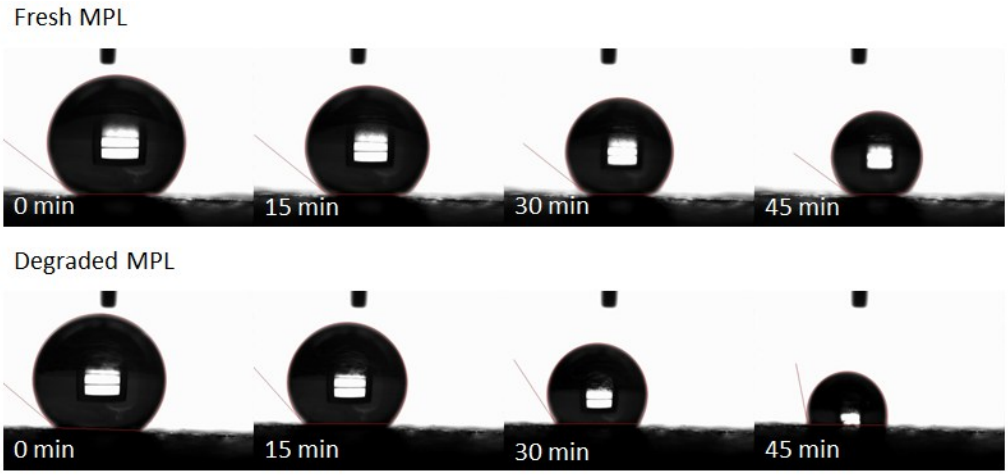

Figure 28: Static contact angle time study for fresh and degraded S2 sample MPL surface.

Specimen	0 min	15 min	30 min	45 min
Fresh	142	140	134	134
Degraded	134°	130°	127°	99°

Table 8: Static contact angle time study for fresh and degraded S2 sample GDL fibers.

Specimen	0 min	15 min	30 min	45 min
Fresh	144°	141°	143°	144°
Degraded	142°	134°	123°	104°

Table 9: Static contact angle time study for fresh and degraded S2 sample MPL surface.

The S3 sample study used the same GDL sample and locations throughout and employed the coordinate system defined in Section 4.2.3. Tables 10 and 11 show the average contact angles measured on the surface of the GDL fiber side and MPL side of the S3 GDL sample respectively.

Specimen	Static	Advancing	Receding
Fresh	137°	143°	139°
Degraded	135°	138°	132°

Table 10: S3 sample fresh GDL fiber surface advancing, receding, and static contact angle study.

Specimen	Static	Advancing	Receding
Fresh	147°	144°	143°
Degraded	136°	136°	136°

Table 11: S3 sample degraded MPL surface advancing, receding, and static contact angle study.

The static contact angle time studies for the S3 sample fresh and degraded GDL fiber surface and MPL surface are pictured in Figures 29 and 30 respectively.

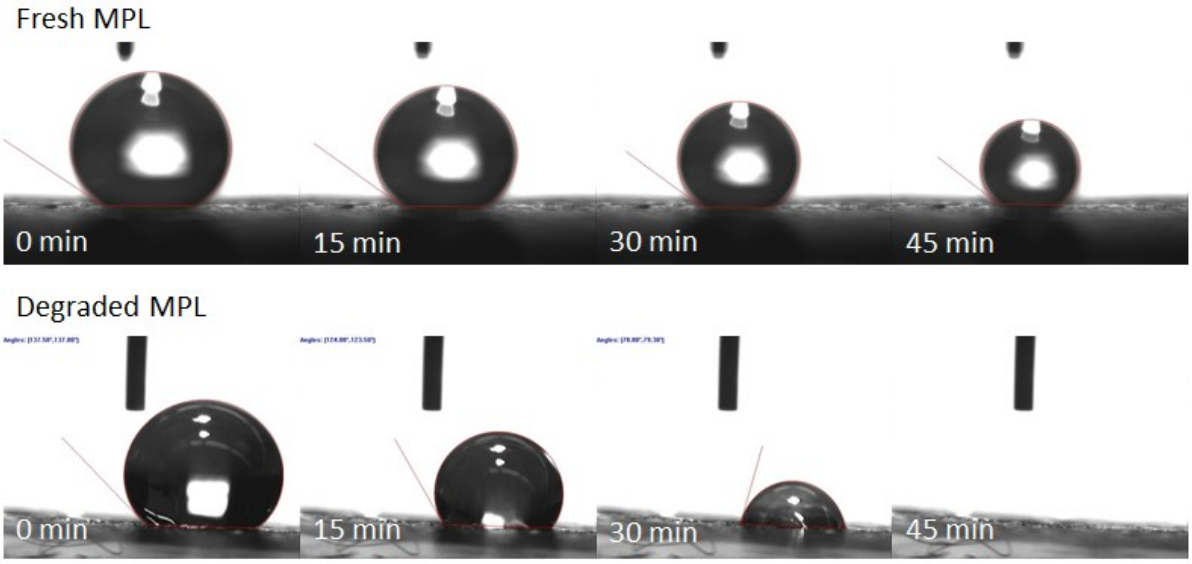

Figure 29: Static contact angle time study for fresh and degraded S3 sample GDL fibers.

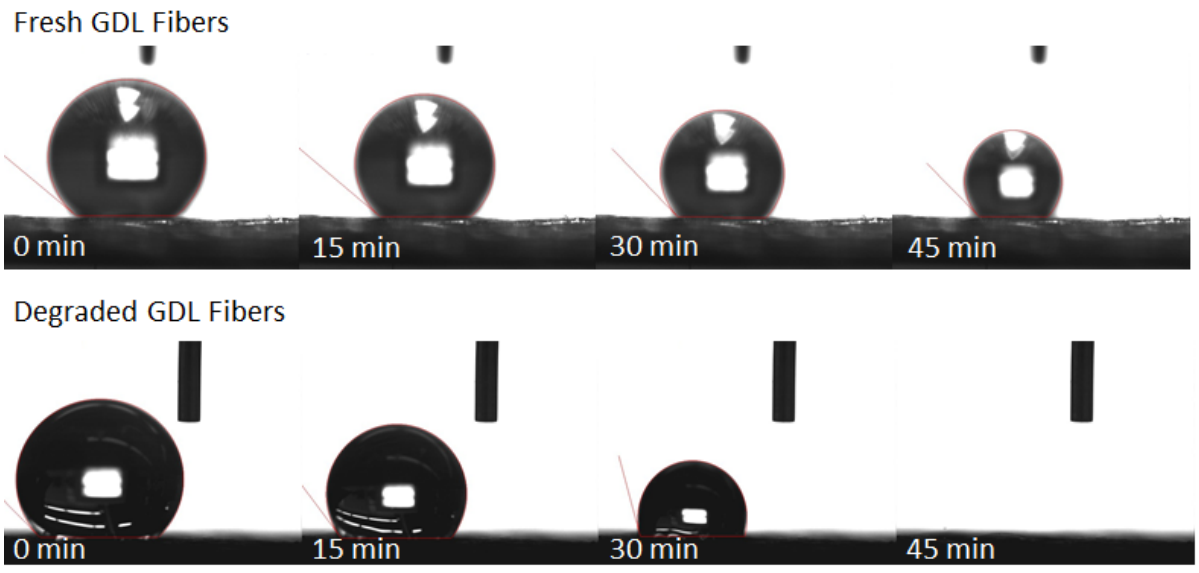

Figure 30: Static contact angle time study for fresh and degraded S3 sample MPL surface.

Table 12 and 13 show the contact angles measured for the S3 sample fresh and degraded GDL fiber surface and MPL surface during the time study.

Specimen	0 min	15 min	30 min	45 min
Fresh	142°	140°	134°	134°
Degraded	137°	129°	107°	0°

Table 12: Static contact angle time study for fresh and degraded S3 sample GDL fibers.

Specimen	0 min	15 min	30 min	45 min
Fresh	146°	145°	145°	143°
Degraded	138°	124°	79°	0°

Table 13: Static contact angle time study for fresh and degraded S3 sample MPL surface.

It can be seen in Figures 29 and 30 that the time study shows that the water droplet was completely gone 45 minutes after it was dispensed. This could be due to a higher evaporation rate caused by an increase in the room temperature. However, similar tests were conducted soon after on the surfaces of a fresh sample for comparison and the water droplet was able to be maintained on the surface for the entire 45 minute time period.

5.3 Surface Morphology Investigation

5.3.1 S1 Sample

After the S1 sample was degraded, it was found that heavy corrosion occurred in the areas of the MPL where the water was passed during the degradation process. This heavy corrosion is shown in the CLSM image in Figure 31.

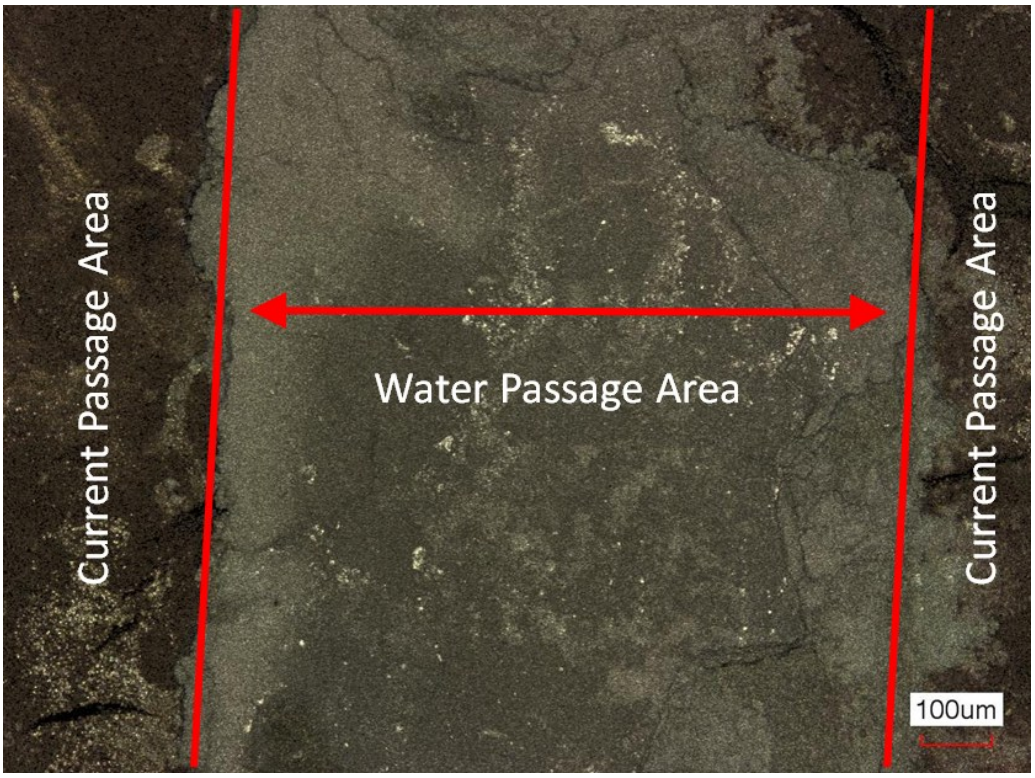

Figure 31: S1 sample high corrosion area.

The light area is where the water was passed and the darker regions are where the CCP lands contacted the sample and passed electric current through it. The corrosion was so heavy in some areas that a distinct height difference was observed between the water and current passage areas. Figure 32 shows a close up CLSM image of the same water and current passage interface. The change in elevation from the corroded water passage area to the current passage area was measured using the software on the CLSM. Three different elevation changes between the water passage and current passage areas were measured on the top, middle, and bottom of the CLSM image in Figure 32. The average height difference was determined to be 55 µm. It can be seen that this thick layer of corrosion completely blocked the MPL cracks and is most likely not permeable to water. The high level of corrosion was only seen on certain parts of the areas where water was passed.

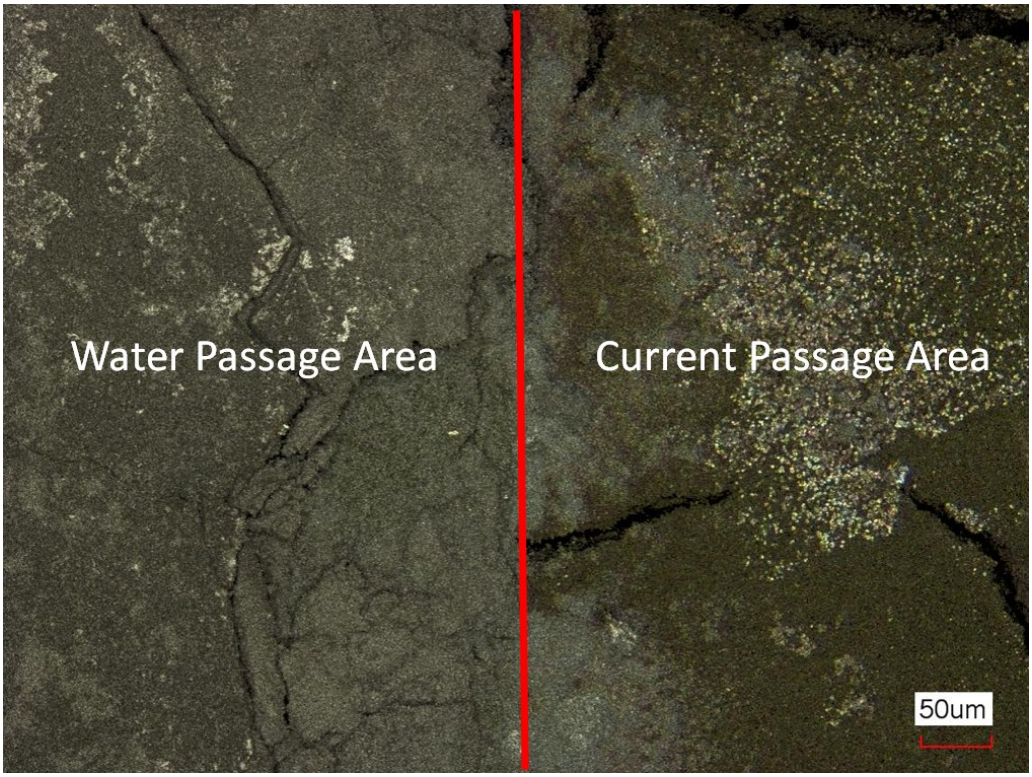

Figure 32: S1 sample high corrosion area close up.

No visible degradation, such as broken fibers from compression, or enlarged pores from continuous water passage was seen on the fiber side of the S1 GDL sample.

5.3.2 S2 Sample

The results gathered from the S1 sample called for more investigation and the S2 sample was more heavily investigated. Figure 33 shows that the corrosion was not as heavy for this sample but was still visible as a distinct change in texture existed between the water passage and current passage areas. This moderate level of corrosion was thought to be due to the fact that the S2 sample was degraded at room temperature rather than at 80 °C like the S1 sample. After investigation, it was suspected that certain cracks in the MPL were blocked by deposits of corrosion as shown in Figure 33. However, these exact same areas were not imaged prior

to exposing the sample to degradation so there was no way to determine whether these were actually deposits or just part of the original surface morphology of the MPL. Thin bridges of material were suspected to have formed in the cracks as pictured in Figure 35.

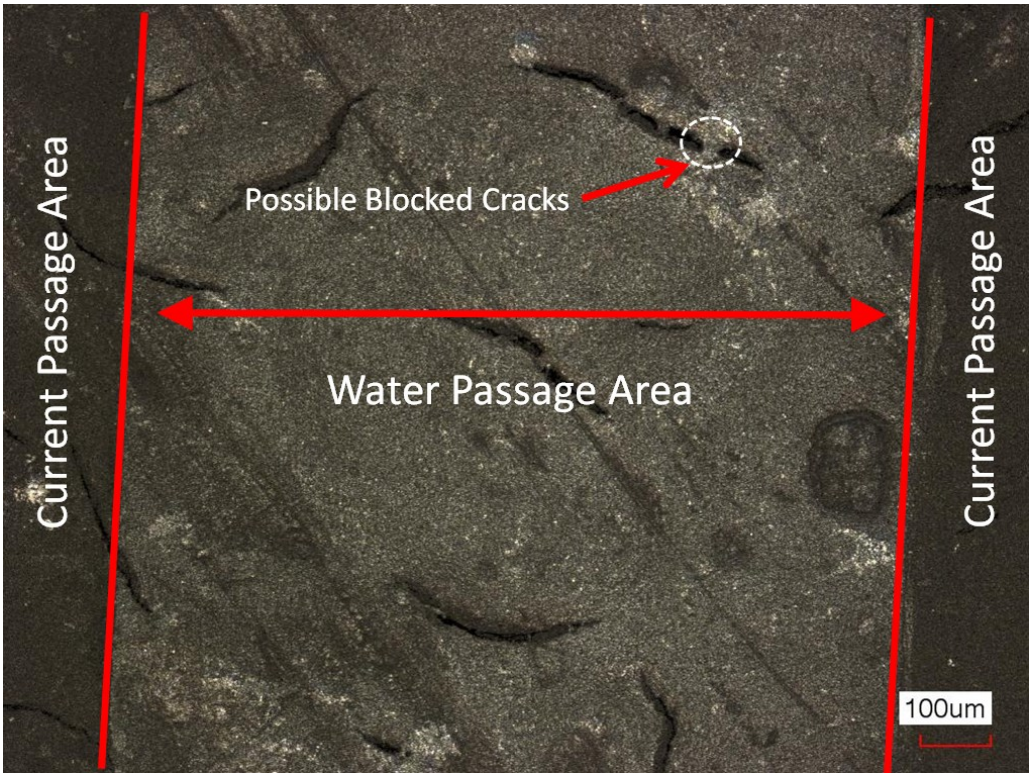

Figure 33: S2 sample moderate corrosion area.

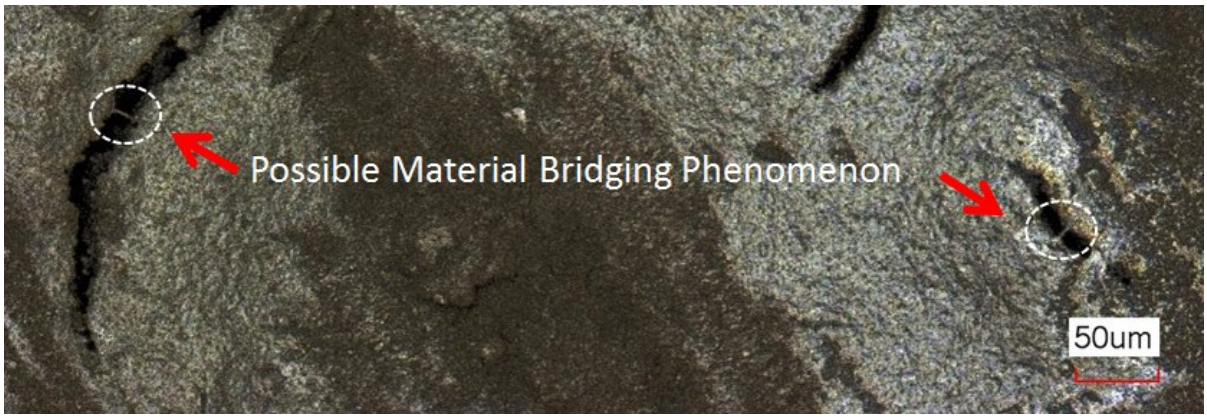

Figure 34: S2 sample small material bridging phenomenon.

Again, no visible degradation was seen on the fiber side of the sample.

5.3.3 S3 Sample

The S3 sample was the first sample to be investigated before and after degradation in the exact same areas using the method discussed in Section 4.2.3. Select areas of both the MPL and fiber side of the S3 sample were investigated. On the MPL side, areas where current was applied and where water was passed were specifically investigated. The first region investigated was where the current was applied. Figures 35 and 36 show CLSM images of this region taken before and after degradation using 10x and 150x objective lenses respectively on the area of interest. There was little change observed in the MPL surface while using the 10x objective lens, but further investigation with the 150x objective lens showed that the bridges did form within the MPL surface cracks. It is apparent that thin bridges of material formed within the MPL surface cracks. Most were at the narrowest portions of the cracks.

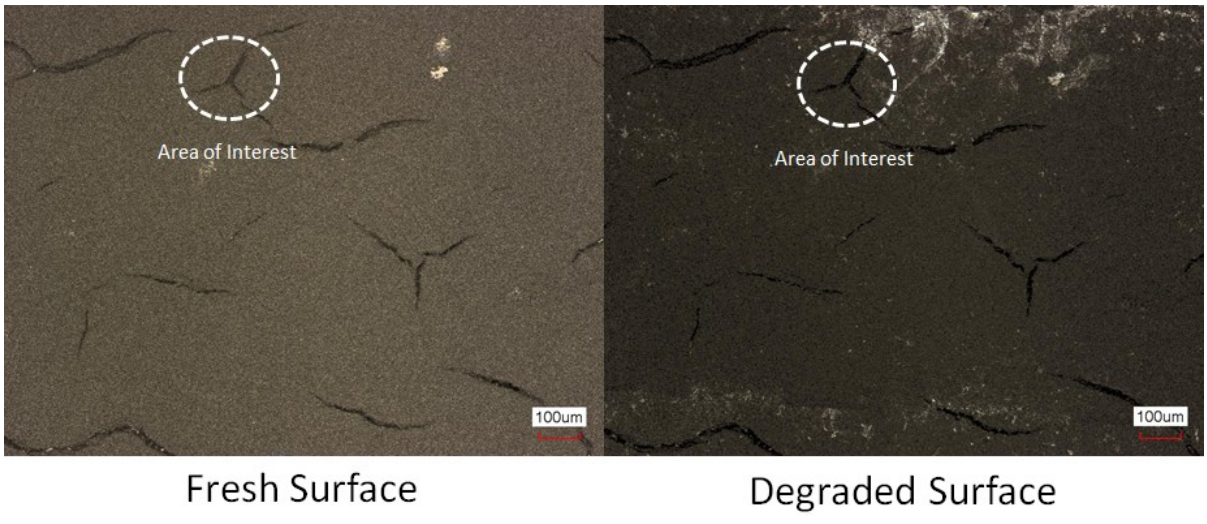

Figure 35: Current application region of the S3 sample MPL surface (10x objective lens).

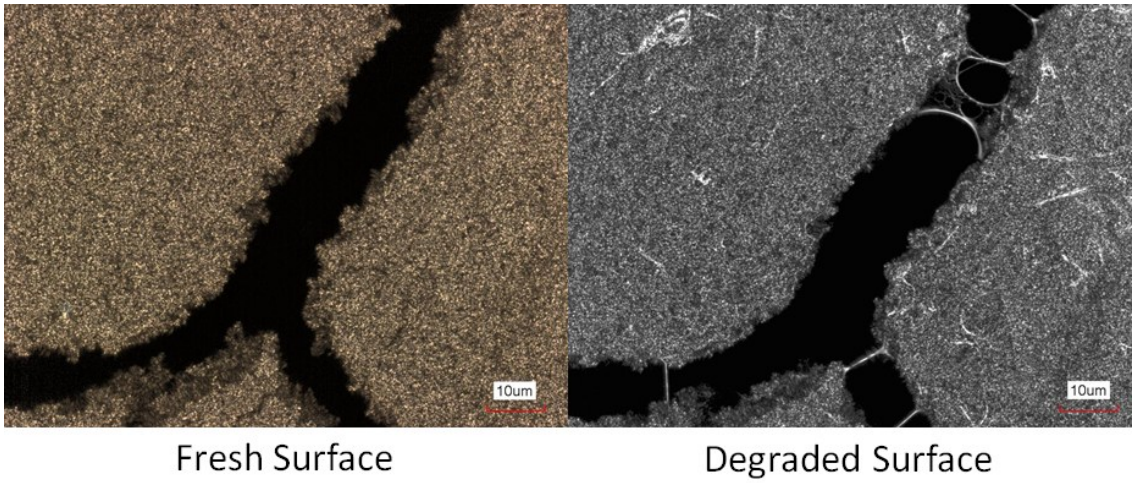

Figure 36: Current application region of the S3 sample MPL surface (150x objective lens).

It can be seen in Figure 37 that much more corrosion deposits were seen in the region where the water was passed. Focusing in on the area of interest in Figure 38 shows much larger material bridges that formed in the surface cracks and large corrosion deposits on the MPL surface. These results show that the water washed areas of the samples suffered from much more corrosion than the areas where current was applied. No extra surface cracks in the MPL formed due to compression and no changes due to shear from the CCP channels were found.

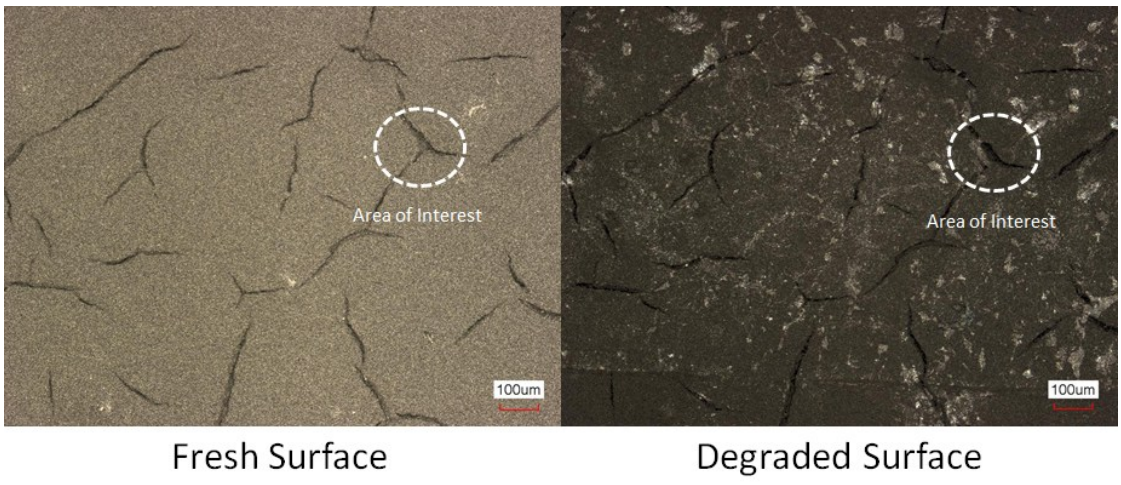

Figure 37: Water washed region of the S3 sample MPL surface (10x objective lens).

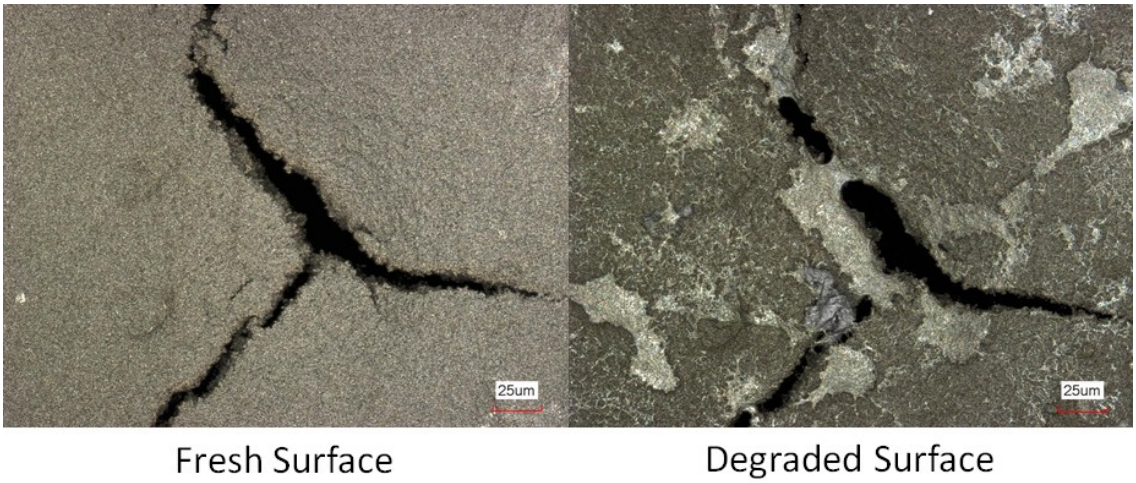

Figure 38: Water washed region of the S3 sample MPL surface (50x objective lens).

Figure 39 shows CLSM images of the fibers before and after degradation using the 10x objective lens. The fiber structures looked exactly the same before and after being exposed to the degradation test. No broken fibers were visible at all throughout the investigation. Focusing in on the area of interest in Figure 39 with the 50x objective lens revealed a section of MPL material as well as a surface crack. This is pictured in Figure 40. Even on the fibrous side of the sample, MPL material and cracks were present. After degradation, these regions showed the same bridging phenomenon seen on the opposite side of the sample. Figure 41 shows the same region magnified even further with a 150x objective lens. The amount of void space taken up by corrosion is vast. It can clearly be seen that the corrosion is only on the MPL and not on the fibers which suggests that the corrosion is caused by the water flowing rather than a universal chemical reaction that occurred throughout the entire GDL sample structures.

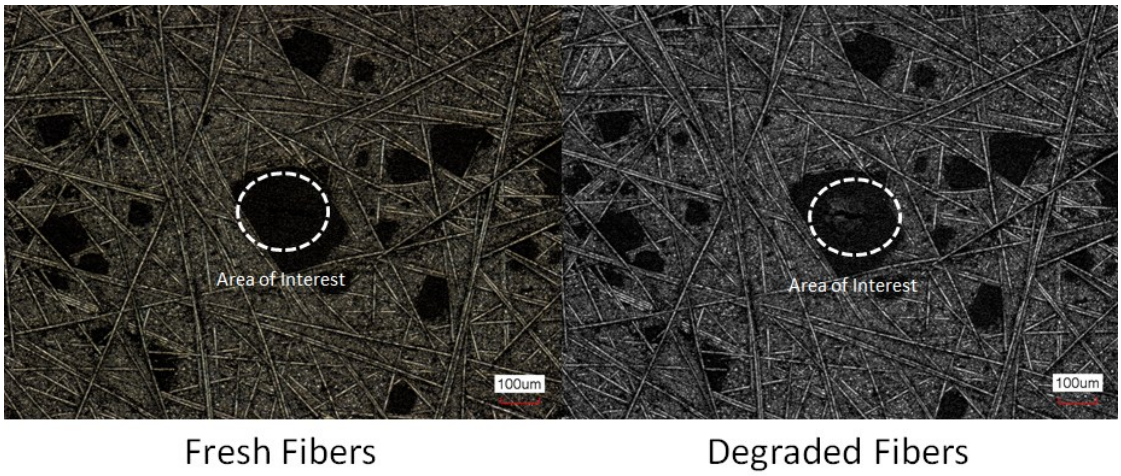

Figure 39: S3 sample GDL fiber structure (10x objective lens).

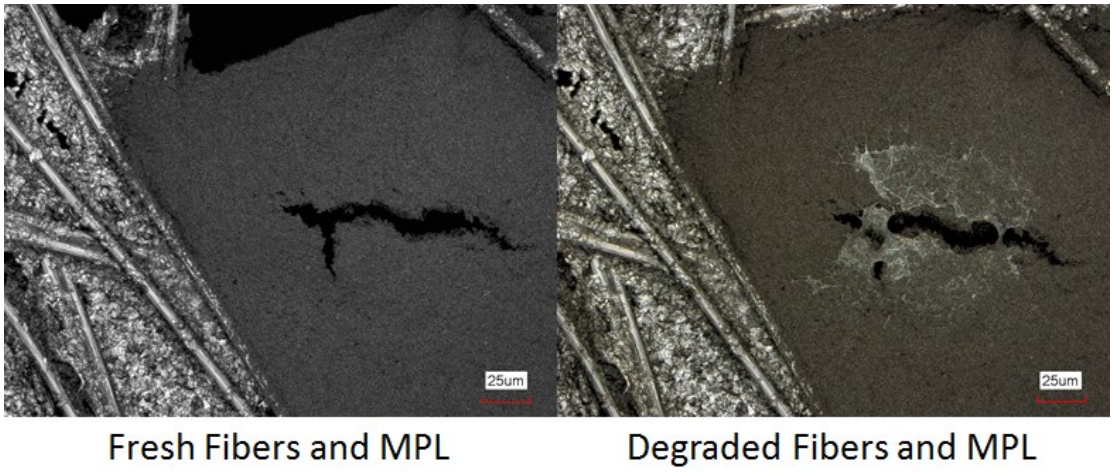

Figure 40: S3 sample GDL fiber structure and portion of MPL (50x objective lens).

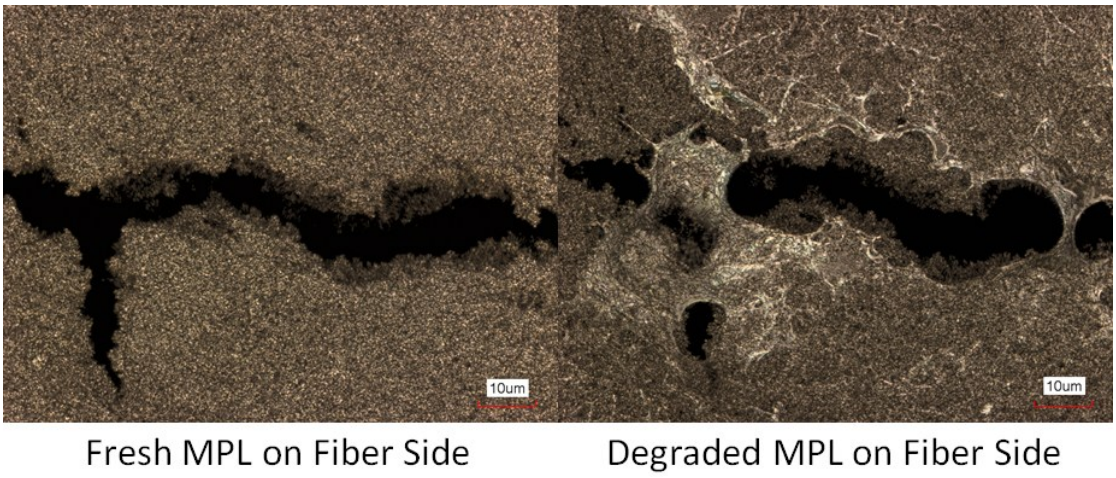

Figure 41: S3 sample portion of MPL on fiber side (150x objective lens).

5.4 Compositional Analysis

A brief compositional analysis was performed on the MPL side of the S3 sample in an effort to try and identify the elements that make up the bridging material that formed. A fresh GDL sample cut from the same sheet as the S3 sample was investigated first. Figure 42 shows that the only elements present in the section of MPL investigated were carbon and fluorine.

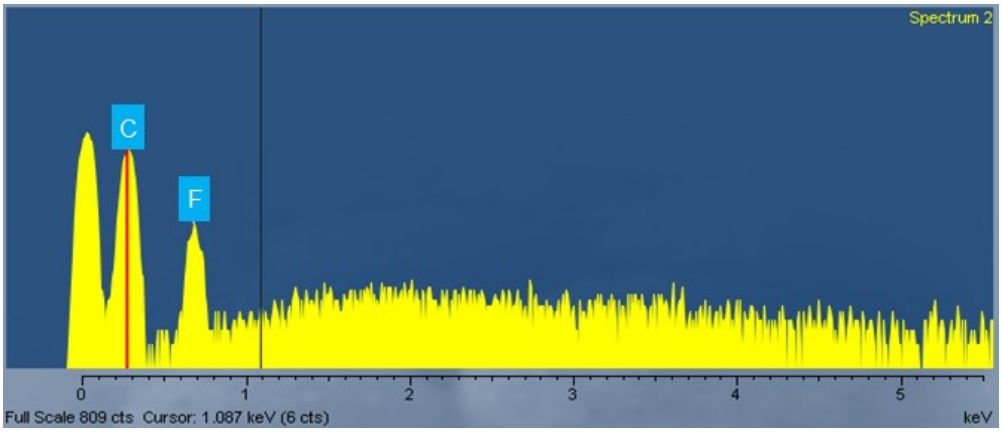

Figure 42: Elemental concentration of a fresh MPL surface.

Subsequently, the degraded S3 sample MPL surface was investigated and Figure 43 shows the two particular material bridges that were focused on for this study.

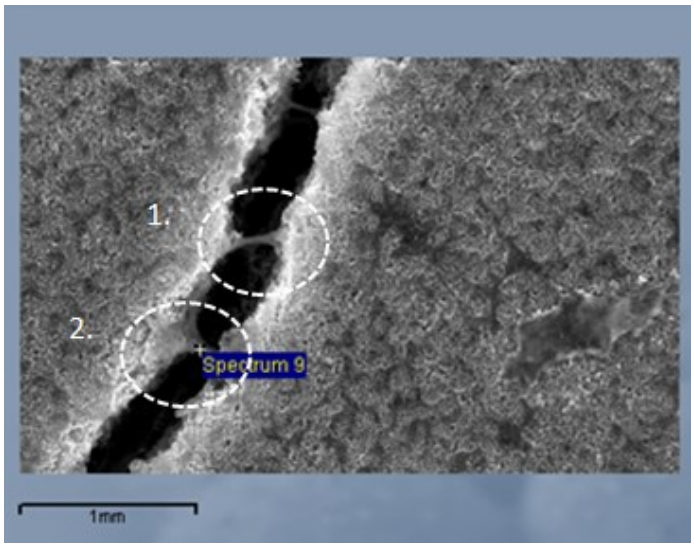

Figure 43: Material bridges that were studied on the degraded S3 sample MPL surface.

Figures 44 and 45 shows that additional elements were possibly present in the two material bridges. Table 14 outlines the elements that were picked up and the likelihood of them actually being present.

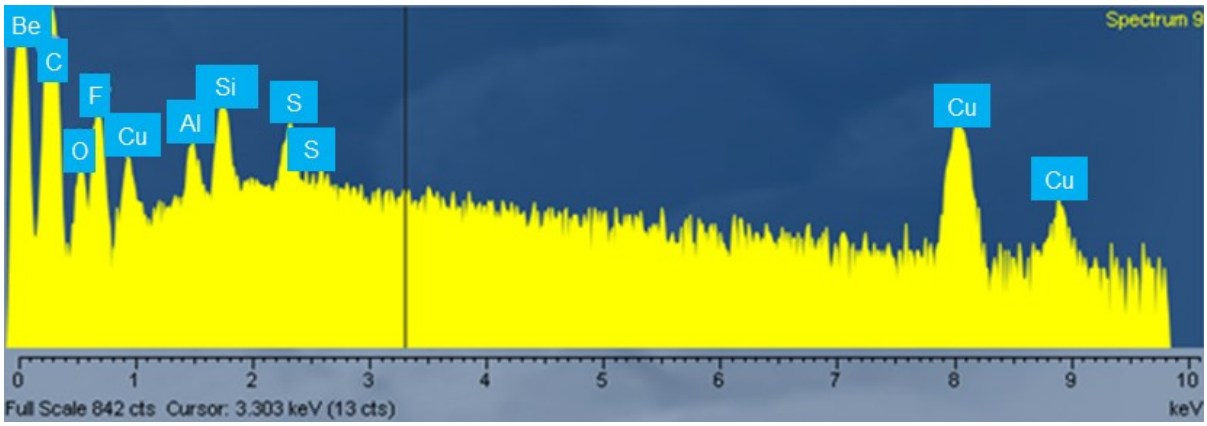

Figure 44: Elemental concentration of the first material bridge on degraded S3 sample MPL surface.

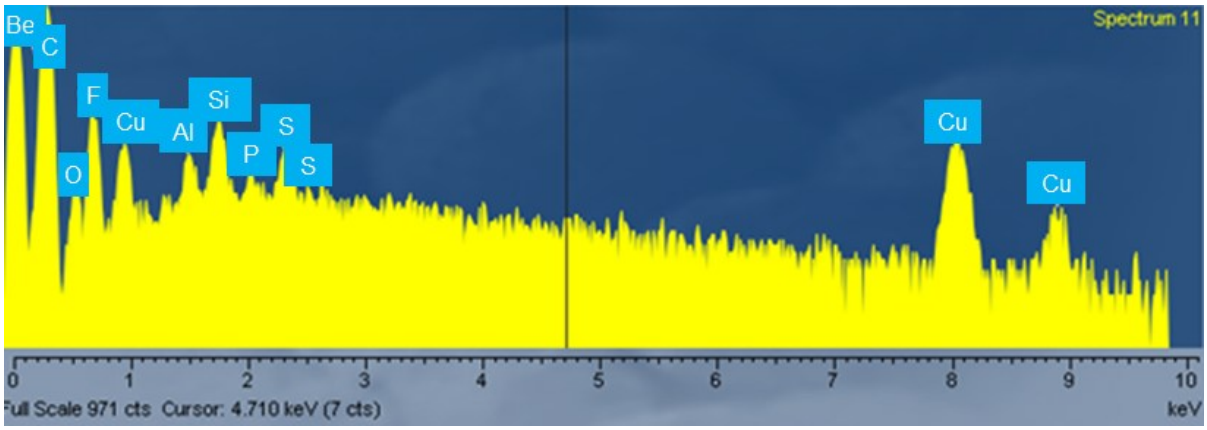

Figure 45: Elemental concentration of the second material bridge on degraded S3 sample MPL surface.

Beryllium was not present in the bridge material as the beryllium peak was caused by the beryllium in the window of the microscope. However, it is very possible that, due to corrosion, oxygen is trapped in the bridge material. Copper was also found to be present and could be due to removing adhesive sealant material that was lodged in the CCP channels

before the S3 sample was degraded. The material was removed with a sharp knife and parts of the gold plating may have come off leaving the bare copper exposed.

Element	Likely Present	Not Likely Present
Beryllium		X
Chlorine	X	
Oxygen	X	
Copper	X	
Silicon	X	
Aluminum	X	
Sulfur	X	
Phosphorus	X	

Table 14: Additional elements found in S3 sample bridging material.

Chlorine and phosphorus could be present due to a bad filter in the DI water system. The sulfur and silicon are most likely from the Permatex® Black Silicone Adhesive Sealant used on the CCP gaskets. Aluminum could be present due to the corrosion of the manifolds by DI water. The gold did not delaminate at all as a result of the degradation test as other areas of the degraded MPL surface were inspected.

5.5 Discussion

The CBP values were decreased due to the degradation test. From Equation (15) it can be seen that capillary pressure is a function of pore radius, surface tension, and contact angle. The surface tension of water in contact with air can be treated as a constant value for these tests as all the CBP measurement tests were conducted at room temperature. The surface

morphology investigation showed that the surface cracks in the MPLs were blocked by corrosion. Should the water actually travel through the cracks of the MPL, these corrosion deposits effectively made the pore radius smaller. However since the MPL surface contact angle decreased, the corrosion areas within the cracks could be locally hydrophilic. This would cause a negative capillary pressure and a droplet pinning site. The surface morphology and contact angle investigations also showed that the pore sizes of the fiber structure did not change yet the contact angle decreased. This confirms theoretically a lower capillary driving force through the GDL fiber structure. Therefore, the corrosion seen on the MPL coupled with the loss of hydrophobicity in the fiber network was the main cause of the CBP decrease.

The disappearance of the DCP exhibited in all but one of the S2 and S3 sample CBP measurement tests suggest that the water remained connected after breaking through the GDL. It is possible that the wicking membrane was no longer able to remove the water from the GDL after breakthrough due to the decrease in the overall hydrophobicity of the GDL fiber network. Water droplets could have gotten pinned within the fibers much easier and, in turn, would be harder for the wicking membrane to remove as they are effectively stuck within the fibers. The drop in pressure to a constant value could indicate that the pressure required to break through the GDL is higher than the pressure needed to steadily transport water through the GDL. However, visualization tools are needed to confirm what is actually occurring simultaneously with the pressure changes.

Degradation time could have had an effect on the DCP change as well. Both the S2 and S3 samples exhibited the possibility of containing an increased amount of hydrophilic pores and regions from the CBP measurement tests while the S1 sample did not. This could be due to the fact that they were both exposed to the degradation tests for a longer time of 500 hours.

Although the S1 sample had more MPL surface corrosion, the GDL fiber network could have been internally more hydrophobic than that of the S2 and S3 samples as it was only subjected to the degradation test for 75 hours.

The heaviest corrosion was seen on the S1 sample which was exposed to high temperatures in its respective degradation test. Most of the corrosion could be due to the highly pure DI water coming into contact with the aluminum manifold channels for prolonged periods of time during the degradation tests. The water comes in contact with air in the channels and contains dissolved oxygen which in turn allows for the corrosion of aluminum to occur. When deaerated water is used, a protective surface film forms on the surface of the aluminum [42]. However, the DI water used for the degradation test was not deaerated as the water produced and used for reactant gas humidification in a real fuel cell contains oxygen. Aluminum is resistant to high purity water at room temperature and a small initial reaction occurs in which a protective oxide film forms and the effect of water on the aluminum becomes negligible [42]. Increasing the temperature has an adverse effect however and aluminum oxide powder can form. This could be what formed the material bridges in the cracks of the MPL as both aluminum and oxygen were found as a result of the compositional analysis. The large white deposits that formed on parts of the MPL surface of the S1 sample could be comprised of aluminum oxide powder. They also completely block the water passageways in certain regions of the S1 sample and water may have been redirected to regions that were still somewhat hydrophobic in nature as the degradation time for this sample was much shorter than the others. The S2 and S3 samples were run at room temperature and a protective oxide film most likely formed within the first ten days of exposure to the DI water [42]. However during this time period, aluminum still can be picked

up by the DI water which is why it was still present in the S2 sample. The manifold channels were cleaned with isopropyl alcohol in between the S2 and S3 degradation tests which removed the protective oxide film that formed and allowed for the same phenomenon to reoccur on the S3 sample.

6. CONCLUSIONS

A method for degrading GDL samples was developed to degrade GDL samples by using a specially designed ex situ test section. The main purpose was to identify the degradation mechanisms inherent to the GDL and their effect on water transport mechanisms within it. SGL 25 BC samples were exposed to compression, electric current, accelerated liquid water flow, and temperature. Water breakthrough behavior was investigated before and after degradation and the CBP values decreased in all of the degraded samples. Based on the presented study, the following conclusions were drawn:

i. The surface morphology investigation showed the presence of corrosion deposits on the MPL surface but not on the fibers. No change in the structure of the fibers was observed.

ii. The surface wettability investigation showed a decrease in contact angle on both the MPL surface and fibrous side. The contact angle decreased drastically when a water droplet was left on the degraded MPL and fiber surfaces over time.

iii. Compositional analysis showed that aluminum oxide formation is most likely the main cause of the corrosion found on the GDL. This could have been mitigated through anodizing the aluminum manifolds.

iv. Because of the corrosion deposits on the MPL cracks and the decrease of hydrophobicity of the fiber network, less hydrophobic pores and regions could have been formed in the GDL samples. This caused degradation in the capillary action inherent to the GDL samples and the CBP measurement data confirms this.

The decrease in hydrophobicity is therefore the degradation mechanism found in this study. In turn, the lower CBP could lead to a flooding condition and mass transport losses at the cathode side of the fuel cell during operation.

The CBP measurement method employed in this study can be applied in industry to characterize GDLs and the different water transport mechanisms inherent to each type. The water breakthrough data and capillary flow characteristics gained through CBP measurement can be correlated with performance data acquired using the same GDL type or sample in an in situ environment. Mass transport losses can possibly be correlated with ex situ generated capillary pressure curves. The method can also be used to characterize hydrophobicity loss in future ex situ degradation studies and possibly carefully conducted in situ studies.

7. FUTURE WORK

This work can be extended by investigating a GDL without an MPL or one that has 0 wt% PTFE on the carbon fibers. The elimination of the wicking membrane and the introduction of air flow on the water breakthrough side of the GDL sample are essential to allow for longer CBP measurements. Using an air flow rate that is similar to what is normally used on the cathode side of a fuel cell could simulate a fuel cell environment even further for the CBP measurement tests.

Employing visualization techniques would also allow for much insight to be gained with respect to the different curves generated as water travels through hydrophobic or hydrophilic regions of the GDL. Visualizing the way water emerges from the GDL into a channel can also provide insight to whether an eruptive water transport mechanism is present and the water is traveling through a hydrophobic pore or if the water is slowly emerging through a hydrophilic pore.

Anodizing the aluminum manifolds would prevent corrosion and would allow a more accurate investigation of the actual degradation of the GDL. Cycling the voltage as well as the temperature could be incorporated into a future degradation test as this may cause increased PTFE loss. Finally, the design of an ex situ test section that accepts a GDL that is the same size as the GDL used in an in situ environment would provide the most insight. With this, GDLs could be effectively degraded by the ex situ test section, be carefully removed, and, in turn, be run in an in situ test to characterize the degradation through the generation of polarization curves. Polarization curves generated using ex situ degraded GDLs could then be compared to GDLs used in in situ operation for extended periods of time to validate the ex situ degradation. The changes in capillary action observed in the degraded

GDLs in the ex situ test section could also be correlated with the mass transport loss region of the polarization curves generated using the same degraded GDLs in an in situ environment.

8. REFERENCES

[1] Mench M., Kumbar E. C., and Veziroglu T. N., 2012, Polymer Electrolyte Fuel Cell Degradation, Elsevier Inc.

[2] O'Hayre R., 2009, Fuel Cell Fundamentals, John Wiley & Sons, Inc.

[3] Mench M., 2008, Fuel Cell Engines, John Wiley & Sons, Inc., Hoboken.

[4] Vielstich W., Lamm A., and Gasteiger, Hubert, 2003, "Fuel Cell Technology and Applications Part 1," Handbook of Fuel Cells, John Wiley & Sons Ltd., West Sussex.

[5] Kandlikar S. G., Garofalo M. L., and Lu Z., 2011, "Water Management in A PEMFC: Water Transport Mechanism and Material Degradation in Gas Diffusion Layers," Fuel Cells, **11**(6), pp. 814–823.

[6] Lu Z., Daino M. M., Rath C., and Kandlikar S. G., 2010, "Water management studies in PEM fuel cells, part III: Dynamic breakthrough and intermittent drainage characteristics from GDLs with and without MPLs," International Journal of Hydrogen Energy, **35**(9), pp. 4222–4233.

[7] Karimi G., Li X., and Teertstra P., 2010, "Measurement of through-plane effective thermal conductivity and contact resistance in PEM fuel cell diffusion media," Electrochimica Acta, **55**(5), pp. 1619–1625.

[8] Sadeghi E., Djilali N., and Bahrami M., 2010, "Effective thermal conductivity and thermal contact resistance of gas diffusion layers in proton exchange membrane fuel cells. Part 2: Hysteresis effect under cyclic compressive load," Journal of Power Sources, **195**(24), pp. 8104–8109.

[9] Khandelwal M., and Mench M. M., 2006, "Direct measurement of through-plane thermal conductivity and contact resistance in fuel cell materials," Journal of Power Sources, **161**(2), pp. 1106–1115.

[10] Wang Y., Wang C.-Y., and Chen K. S., 2007, "Elucidating differences between carbon paper and carbon cloth in polymer electrolyte fuel cells," Electrochimica Acta, **52**(12), pp. 3965–3975.

[11] Kandlikar S. G., Lu Z., Lin T. Y., Cooke D., and Daino M., 2009, "Uneven gas diffusion layer intrusion in gas channel arrays of proton exchange membrane fuel cell and its effects on flow distribution," Journal of Power Sources, **194**(1), pp. 328–337.

[12] Gostick J. T., Fowler M. W., Ioannidis M. A., Pritzker M. D., Volfkovich Y. M., and Sakars A., 2006, "Capillary pressure and hydrophilic porosity in gas diffusion layers for polymer electrolyte fuel cells," Journal of Power Sources, **156**(2), pp. 375–387.

[13] Quick C., Ritzinger D., Lehnert W., and Hartnig C., 2009, "Characterization of water transport in gas diffusion media," Journal of Power Sources, **190**(1), pp. 110–120.

[14] Owejan J. P., Gagliardo J. J., Sergi J. M., Kandlikar S. G., and Trabold T. A., 2009, "Water management studies in PEM fuel cells, Part I: Fuel cell design and in situ water distributions," International Journal of Hydrogen Energy, **34**(8), pp. 3436–3444.

[15] Borup R., Meyers J., Pivovar B., Kim Y. S., Mukundan R., Garland N., Myers D., Wilson M., Garzon F., Wood D., Zelenay P., More K., Stroh K., Zawodzinski T., Boncella J., McGrath J. E., Inaba M., Miyatake K., Hori M., Ota K., Ogumi Z., Miyata S., Nishikata A., Siroma Z., Uchimoto Y., Yasuda K., Kimijima K., and Iwashita N., 2007, "Scientific Aspects of Polymer Electrolyte Fuel Cell Durability and Degradation," Chemical Reviews, **107**(10), pp. 3904–3951.

[16] Larminie J., and Dicks A., 2003, Fuel Cell Systems Explained, John Wiley & Sons Ltd., West Sussex.

[17] Bear J., 1972, Dynamics of Fluids in Porous Media, Dover Publications, Inc., Mineola.

[18] Sinha P. K., and Wang C.-Y., 2007, "Pore-network modeling of liquid water transport in gas diffusion layer of a polymer electrolyte fuel cell," Electrochimica Acta, **52**(28), pp. 7936–7945.

[19] Udell K. S., 1985, "Heat transfer in porous media considering phase change and capillarity—the heat pipe effect," International Journal of Heat and Mass Transfer, **28**(2), pp. 485–495.

[20] Zhang S., Yuan X., Wang H., Merida W., Zhu H., Shen J., Wu S., and Zhang J., 2009, "A review of accelerated stress tests of MEA durability in PEM fuel cells," International Journal of Hydrogen Energy, **34**(1), pp. 388–404.

[21] Bazylak A., Sinton D., and Djilali N., 2008, "Dynamic water transport and droplet emergence in PEMFC gas diffusion layers," Journal of Power Sources, **176**(1), pp. 240–246.

[22] Gostick J. T., Ioannidis M. A., Fowler M. W., and Pritzker M. D., 2008, "Direct measurement of the capillary pressure characteristics of water–air–gas diffusion layer systems for PEM fuel cells," Electrochemistry Communications, **10**(10), pp. 1520–1523.

[23] Liu T.-L., and Pan C., 2012, "Visualization and back pressure analysis of water transport through gas diffusion layers of proton exchange membrane fuel cell," Journal of Power Sources, **207**(0), pp. 60–69.

[24] Lee C., and Mérida W., 2007, "Gas diffusion layer durability under steady-state and freezing conditions," Journal of Power Sources, **164**(1), pp. 141–153.

[25] Chen G., Zhang H., Ma H., and Zhong H., 2009, "Electrochemical durability of gas diffusion layer under simulated proton exchange membrane fuel cell conditions," International Journal of Hydrogen Energy, **34**(19), pp. 8185–8192.

[26] Wu J., Yuan X. Z., Martin J. J., Wang H., Zhang J., Shen J., Wu S., and Merida W., 2008, "A review of PEM fuel cell durability: Degradation mechanisms and mitigation strategies," Journal of Power Sources, **184**(1), pp. 104–119.

[27] Borup R., Inbody M., Davey J., Wood D., Fernando G., Tafoya J., Xie J., and Pacheco S., 2004, "PEM Fuel Cell Durability."

[28] Bazylak A., Sinton D., Liu Z.-S., and Djilali N., 2007, "Effect of compression on liquid water transport and microstructure of PEMFC gas diffusion layers," Journal of Power Sources, **163**(2), pp. 784–792.

[29] Kim S., Ahn B. K., and Mench M. M., 2008, "Physical degradation of membrane electrode assemblies undergoing freeze/thaw cycling: Diffusion media effects," Journal of Power Sources, **179**(1), pp. 140–146.

[30] Mukundan R., Kim Y. S., Garzon F. H., and Pivovar B., 2006, "Freeze/Thaw Effects in PEM Fuel Cells," ECS Trans., **1**(8), pp. 403–413.

[31] Lin J.-H., Chen W.-H., Su S.-H., Su Y.-J., and Ko T.-H., 2008, "Washing Experiment of the Gas Diffusion Layer in a Proton-Exchange Membrane Fuel Cell," Energy Fuels, **22**(4), pp. 2533–2538.

[32] Owejan J. E., Yu P. T., and Makharia R., 2007, "Mitigation of Carbon Corrosion in Microporous Layers in PEM Fuel Cells," ECS Trans., **11**(1), pp. 1049–1057.

[33] Gurau V., Mann J. A., Zawodzinski T., Larson J., and Hicks M., 2008, "Effect of the GDL Degradation on its Transport Properties," Meet. Abstr. - Electrochem. Soc.,

801(11), p. 477.

[34] Aoki T., Matsunaga A., Ogami Y., Maekawa A., Mitsushima S., Ota K., and Nishikawa H., 2010, "The influence of polymer electrolyte fuel cell cathode degradation on the electrode polarization," Journal of Power Sources, **195**(8), pp. 2182–2188.

[35] Wu J., Martin J. J., Orfino F. P., Wang H., Legzdins C., Yuan X.-Z., and Sun C., 2010, "In situ accelerated degradation of gas diffusion layer in proton exchange membrane fuel cell: Part I: Effect of elevated temperature and flow rate," Journal of Power Sources, **195**(7), pp. 1888–1894.

[36] Lim S.-J., Park G.-G., Park J.-S., Sohn Y.-J., Yim S.-D., Yang T.-H., Hong B. K., and Kim C.-S., 2010, "Investigation of freeze/thaw durability in polymer electrolyte fuel cells," International Journal of Hydrogen Energy, **35**(23), pp. 13111–13117.

[37] Schulze M., Wagner N., Kaz T., and Friedrich K. A., 2007, "Combined electrochemical and surface analysis investigation of degradation processes in polymer electrolyte membrane fuel cells," Electrochimica Acta, **52**(6), pp. 2328–2336.

[38] Schulze M., and Christenn C., 2005, "XPS investigation of the PTFE induced hydrophobic properties of electrodes for low temperature fuel cells," Applied Surface Science, **252**(1), pp. 148–153.

[39] Cho J., Ha T., Park J., Kim H.-S., Min K., Lee E., and Jyoung J.-Y., 2011, "Analysis of transient response of a unit proton-exchange membrane fuel cell with a degraded gas diffusion layer," International Journal of Hydrogen Energy, **36**(10), pp. 6090–6098.

[40] Dhanushkodi S., Fowler M., Pritzker M., Yuan X.-Z., and Wang H., 2010, "Degradation and Diagnostic Analysis of Gas Diffusion Layers under Humidity Cycling."

[41] Atiyeh H. K., Karan K., Peppley B., Phoenix A., Halliop E., and Pharoah J., 2007,

"Experimental investigation of the role of a microporous layer on the water transport and performance of a PEM fuel cell," Journal of Power Sources, **170**(1), pp. 111–121.

[42] Davis J. R., 1999, Corrosion of Aluminum and Aluminum Alloys, ASM International®, Materials Park.